Monthly Notices
of the
ROYAL ASTRONOMICAL SOCIETY

MNRAS 445, 4287–4305 (2014) doi:10.1093/mnras/stu2029

New *PARSEC* evolutionary tracks of massive stars at low metallicity: testing canonical stellar evolution in nearby star-forming dwarf galaxies

Jing Tang,[1]★ Alessandro Bressan,[1] Philip Rosenfield,[2] Alessandra Slemer,[2] Paola Marigo,[2] Léo Girardi[3] and Luciana Bianchi[4]

[1]*SISSA, via Bonomea 265, I-34136 Trieste, Italy*
[2]*Dipartimento di Fisica e Astronomia Galileo Galilei, Università di Padova, Vicolo dell'Osservatorio 3, I-35122 Padova, Italy*
[3]*Osservatorio Astronomico di Padova, Vicolo dell'Osservatorio 5, I-35122 Padova, Italy*
[4]*Department of Physics, and Astronony, The Johns Hopkins University, 407 Bloomberg Center, 3400 N Charles St, Baltimore, MD 21218, USA*

Accepted 2014 September 26. Received 2014 September 25; in original form 2014 August 8

ABSTRACT

We extend the *PARSEC* library of stellar evolutionary tracks by computing new models of massive stars, from 14 to 350 $M_\odot$. The input physics is the same used in the *PARSEC* V1.1 version, but for the mass-loss rate from considering the most recent updates in the literature. We focus on low metallicity, $Z = 0.001$ and $Z = 0.004$, for which the metal-poor dwarf irregular star-forming galaxies, Sextans A, the Wolf–Lundmark–Melotte galaxy and NGC 6822, provide simple but powerful workbenches. The models reproduce fairly well the observed colour-magnitude diagrams (CMDs) but the stellar colour distributions indicate that the predicted blue loop is not hot enough in models with a canonical extent of overshooting. In the framework of a mild extended mixing during central hydrogen burning, the only way to reconcile the discrepancy is to enhance the overshooting at the base of the convective envelope (EO) during the first dredge-up. The mixing scales required to reproduce the observed loops, EO $= 2H_P$ or EO $= 4H_P$, are definitely larger than those derived from, e.g. the observed location of the red-giant-branch bump in low mass stars. This effect, if confirmed, would imply a strong dependence of the mixing scale below the formal Schwarzschild border, on the stellar mass or luminosity. Reproducing the features of the observed CMDs with standard values of envelope overshooting would require a metallicity significantly lower than the values measured in these galaxies. Other quantities, such as the star formation rate and the initial mass function, are only slightly sensitive to this effect. Future investigations will consider other metallicities and different mixing schemes.

Key words: stars: evolution – Hertzsprung–Russell and colour-magnitude diagrams – stars: interiors – stars: massive.

1 INTRODUCTION

The PADOVA database of stellar evolutionary tracks and isochrones has been continuously updated during recent decades (Girardi et al. 2002; Marigo et al. 2008; Bertelli et al. 2009), except for the models of the most massive stars ($M > 20$ $M_\odot$), which have remained untouched for two decades, after Bertelli et al. (1994). In the most recent major revision, all the basic input physics was revisited and updated, and additions were introduced, such as the pre-main-sequence phase and very low mass stellar models ($0.35 \geq M \geq 0.1$ $M_\odot$). *PARSEC* (Padova Trieste Stellar Evolution Code) is described in detail in Bressan et al. (2012, 2013) and Chen et al. (2014a). The PADOVA database is one of the most widely used sources of stellar evolutionary tracks and the *PARSEC* revision is not complete without including models of the most massive stars. With the aim of completing the library of stellar evolutionary tracks and isochrones computed with *PARSEC*, we present the calculations of new evolutionary tracks of massive stars, from 14 to 350 $M_\odot$.[1] In this paper, the first of a series devoted to the evolution of massive stars using *PARSEC*, we deal with low metallicity environments. We present the new evolutionary tracks, and we perform preliminary comparisons with the observed colour-magnitude diagrams (CMDs). These tests are fundamental for validating the new models. Models with other values of metallicity are being calculated and will be presented in future works.

★E-mail: tang@sissa.it

[1]The new updated and homogeneous sets of evolutionary tracks, from very low ($M = 0.1$ $M_\odot$) to very massive ($M = 350$ $M_\odot$) stars, are available at http://stev.oapd.inaf.it.

Understanding the evolution of massive stars at low metallicity is particularly relevant, as these stars drive the chemical and dynamical evolution of the surrounding medium, and are a key ingredient in modelling galaxy evolution at early times (Woosley & Heger 2012; Groh et al. 2013). An advantage of studying massive stars at low metallicity is also that, in the very local Universe, star formation is sparkling in gas-rich galaxies, which are also metal poor. In recent decades, the high spatial resolution of the space-borne *Hubble Space Telescope* (*HST*) and the collecting power of 8-m telescopes on the ground have provided accurate photometry of individual stars in these galaxies, and metallicity estimates of young stars and gas from spectroscopy. Such data enable comparison of observed CMDs with model simulations at known metallicity, an important test of how the canonical theory of evolution of massive and intermediate mass stars performs at low metallicity.

The internal evolution of massive stars is affected by two complex physical phenomena for which there is still a significant lack of knowledge. The first is the mass-loss rate, which becomes important in the domain of the very massive stars (initial mass $M \gtrsim 30$ M$_\odot$ depending on metallicity). The second is internal mixing, usually from either differential rotation or convective overshooting. Both effects play an important role in stellar evolution because they may significantly modify the structure of the stars in an irreversible way and so their further evolution. Among the observational quantities that are most sensitive to internal mixing are the predicted surface abundance ratios of CNO elements (Martins & Palacios 2013; Bouret et al. 2013). In massive stars the surface abundances can be affected by mixing during the hydrogen-burning phases and by the eventual subsequent first dredge-up. However, the comparison of model predictions with observed surface abundances still shows significant discrepancies (Maeder et al. 2014). Another interesting effect of mixing in this mass interval is the location in the CMD and duration of the blue loops, where the stars spend a fraction of their central helium-burning lifetime. The morphology and star population of the blue and red helium-burning sequences (BHeBS and RHeBS) may depend on several other parameters, such as the ^{12}C(α, γ)^{16}O reaction rate (Iben 1966; Bertelli, Bressan & Chiosi 1985; Brunish & Becker 1990), and the ^{14}N(p, γ)^{15}O reaction rate (Xu & Li 2004; Weiss et al. 2005; Halabi, El Eid & Champagne 2012), but the most important parameters are the efficiency of mixing in the convective core (Bertelli et al. 1985) and below the convective envelope (Alongi et al. 1991; Godart, Noels & Scuflaire 2013).

While the analysis of surface abundances provides a detailed view of individual stars, the analysis of the stellar distribution across a CMD provides a complementary view of the duration of evolutionary phases over a broad range of masses. The latter requires complete, well-studied and populous stellar samples. In this paper we use published photometry of three star-forming dwarf galaxies in the Local Group, which have hundreds of thousands of resolved individual stars down to intermediate mass stars, to build the observed CMDs for comparison with our new models. In Section 2 we describe the new stellar evolutionary tracks of massive stars calculated with *PARSEC*. Apart from the inclusion of mass loss, which had not been considered in stars less massive than $M = 12$ M$_\odot$, the other parameters are the standard ones in the published tracks (Bressan et al. 2012). However, having in mind the comparison with observed CMDs, we present here also models with enhanced envelope overshooting, which is known to favour more extended blue loops during central He burning. In Section 3 we briefly describe the comparison data used, and estimate the contamination by foreground Milky Way (MW) stars. This is significant only in NGC 6822, which is at low Galactic latitude. The adopted CMD simulation technique is outlined in Section 4. Attenuation by interstellar dust is accounted for using results from the multi-band photometry by Bianchi et al. (2012b). The comparison of the canonical model predictions with the observed CMDs of three selected galaxies, Sextans A, the Wolf–Lundmark–Melotte galaxy (WLM) and NGC 6822, is discussed in Section 5 while those based on models with enhanced envelope overshooting are shown in Section 6. The main conclusions drawn from these comparisons are outlined in Section 7.

2 NEW EVOLUTIONARY TRACKS OF MASSIVE STARS WITH *PARSEC*

The largest value of initial mass in the previously published set of evolutionary tracks computed with *PARSEC* V1.1 is $M = 12$ M$_\odot$. The corresponding hydrogen-burning lifetime is about 15 Myr. To simulate younger and most massive stars we usually resort to our previous database (Bressan et al. 1993; Fagotto et al. 1994a,b,c). Since our stellar evolution code has been deeply revised recently (Girardi et al. 2000; Bressan et al. 2012, 2013), we present here new sets of evolutionary tracks of massive stars computed with the *PARSEC* code. The masses range from $M = 14$ to 350 M$_\odot$ and the evolution is followed from the pre-main-sequence phase to the beginning of the carbon-burning phase. Together with the already published stellar evolution tracks, the database now includes updated and homogeneous sets of evolutionary tracks from very low ($M = 0.1$ M$_\odot$) to very massive ($M = 350$ M$_\odot$) stars, from pre-main sequence to the beginning of central carbon burning. Here we describe the models with low metallicity, $Z = 0.001$ to $Z = 0.004$, which will be used in the following sections to build simulated CMDs for comparison with those of three dwarf irregular galaxies of similar metallicity. Models for lower and higher metallicity will be presented and discussed in a forthcoming paper.

2.1 Basic physics input

The *PARSEC* code is extensively discussed in Bressan et al. (2012, 2013) and Chen et al. (2014a); here we briefly describe the most important updates. The equation of state is computed with the FreeEOS code (A. W. Irwin[2]). Opacities in the high-temperature regime, $4.2 \leq \log(T/\mathrm{K}) \leq 8.7$, are obtained from the Opacity Project At Livermore (Iglesias & Rogers 1996), while in the low-temperature regime, $3.2 \leq \log(T/\mathrm{K}) \leq 4.1$, we use opacities generated with our ÆSOPUS[3] code (Marigo & Aringer 2009). Conductive opacities are included following Itoh et al. (2008). The nuclear reaction network consists of the p-p chains, the CNO tri-cycle, the Ne–Na and Mg–Al chains and the most important α-capture reactions, including the α-n reactions. The reaction rates and the corresponding Q-values are taken from the recommended rates in the JINA database (Cyburt et al. 2010). Electron screening factors for all reactions are from Dewitt, Graboske & Cooper (1973) and Graboske et al. (1973). Energy losses by electron neutrinos are taken from Munakata, Kohyama & Itoh (1985), Itoh & Kohyama (1983) and Haft, Raffelt & Weiss (1994). The outer boundary conditions are discussed in Chen et al. (2014a). The reference solar partition of heavy elements is taken from Caffau et al. (2011), who revised a few species of the Grevesse & Sauval (1998) compilation. According to Caffau et al. (2011), the present-day Sun's metallicity is $Z_\odot = 0.01524$, intermediate between the most recent estimates, e.g. $Z_\odot = 0.0141$

[2] http://freeeos.sourceforge.net/

[3] http://stev.oapd.inaf.it/aesopus

of Lodders, Palme & Gail (2009) and $Z_\odot = 0.0134$ of Asplund et al. (2009), and the previous value of $Z_\odot = 0.017$ by Grevesse & Sauval (1998).

2.2 Convection and mixing

Convective energy transport is described according to the mixing-length theory of Böhm-Vitense (1958), with the mixing length parameter $\alpha_{\rm MLT}$ calibrated on the solar model, $\alpha_{\rm MLT} = 1.74$. The location of the boundary of the convective core of massive stars is estimated according to Bressan, Chiosi & Bertelli (1981), taking into account overshooting from the central unstable region. As thoroughly described in Bressan et al. (2013), the main parameter describing core overshooting is the mean free path of convective elements *across* the border of the unstable region, expressed in units of pressure scale height, $l_c = \Lambda_c H_P$. The overshooting parameter used in the core, $\Lambda_c = 0.5$, is the result of the calibration obtained by the analysis of intermediate age clusters (Girardi, Rubele & Kerber 2009) as well as individual stars (Kamath et al. 2010; Deheuvels et al. 2010; Torres et al. 2014). Note that the overshooting region obtained with this formalism extends over about $0.5 l_c$ *above* the unstable region. Instability against convection is tested with the Schwarzschild criterion. An alternative criterion is that of Ledoux, which takes into account also the effects of the gradient in the mean molecular weight. Without overshooting, using the Ledoux criterion instead of the Schwarzschild one leads to significant differences in the structure of the models and in their evolution, mainly because the size of the semi-convective regions above the unstable core depends on the adopted criterion (Chiosi & Summa 1970). On the other hand, with sizable convective overshooting, the difference between models computed with the two different criteria is significantly reduced. In the present work we opt for the Schwarzschild criterion, which is more appropriate for accounting for the effects of thermal dissipation, according to Kato (1966).

Overshooting at the base of the convective envelope (EO) can also give rise to sizable extra mixing. In the past, two important observational effects have been related to this phenomenon, the location of the bump in the red giant branch (RGB) of low mass stars (the RGB bump seen in the CMD of globular clusters and old open clusters) and the extent of the blue loops of intermediate mass stars (Alongi et al. 1991). Both features have been found to be best explained by a moderate amount of overshooting *below the border of the unstable region*, for about EO = 0.25–1.0, in units of H_P. More recently a similar mechanism has been invoked to improve the agreement with the physical state of matter in the convective–radiative transition region derived from solar oscillation data (Christensen-Dalsgaard et al. 2011). The standard value for intermediate and massive stars used in *PARSEC* V1.1 is EO = $0.7 H_P$. However, as we will see later, with this value it turns out to be difficult to reproduce the extended blue loops seen in the metal-poor dwarf galaxies, therefore we have computed two additional sets of models increasing EO to match the observed extended blue loops. We adopted EO = $2H_P$ and EO = $4H_P$. These additional sets will be discussed in Section 2.5.

2.3 Mass-loss rates

Mass loss is not considered for masses below 12 $M_\odot$ in the *PARSEC* V1.1 tracks, but it cannot be neglected for larger masses. In this section we describe the algorithm used for the new sets of massive star models, obtained by combining several prescriptions found in the literature for the different spectral types.

For the blue supergiant phases ($T_{\rm eff} \geq 12\,000$ K), we adopt the relations provided by Vink, de Koter & Lamers (2000, 2001). This formulation, which we name $R_{\rm V01}$, has an overall dependence of the mass-loss rate on the metallicity of the kind $\dot{M} \propto (Z/Z_\odot)^{0.85}\,M_\odot\,{\rm yr}^{-1}$. For red supergiant stars ($T_{\rm eff} < 12\,000$ K), we adopt the relations provided by de Jager, Nieuwenhuijzen & van der Hucht (1988), $R_{\rm dJ}$. We assume the same dependence on the surface metallicity as in $R_{\rm V01}$. In the Wolf–Rayet phases, we use the Nugis & Lamers (2000) formalism, with its own dependence on the stellar metallicity ($R_{\rm NL}$).

A relevant aspect for the more massive stars concerns the transition from the O-type phase to the luminous blue variable and red supergiant phases and finally to the Wolf–Rayet phase and, equally important, the dependence of this transition upon the surface metallicity of the star. In Bressan et al. (1993), as an example of the Padova models, but generally also in evolutionary computations made by other groups, the transition to the super-wind phase corresponding to the luminous blue variable stage is artificially set when the models cross the Humphreys & Davidson (1979) instability limit in the Hertzsprung–Russell (HR) diagram. During this phase, at solar metallicity, the mass-loss rates reach values of $\dot{M} \simeq 10^{-3}\,M_\odot\,{\rm yr}^{-1}$. In the previous Padova models this limit is set independently from the metallicity of the galaxy, though the mass-loss rates themselves do depend on the abundance of heavy elements as indicated above. More recently, however, the behaviour of the mass-loss rates around this transition has been thoroughly analysed by Gräfener & Hamann (2008) and by Vink et al. (2011). They find that the mass-loss rates are strongly enhanced when the stars approach the Eddington limit,

$$\Gamma = \frac{kL}{4\pi cGM} = 1 \qquad (1)$$

where the symbols have their usual meaning. We have thus included in our formalism the explicit dependence of the mass-loss rates on the ratio of the star luminosity to the corresponding Eddington luminosity, Γ, as described by Vink et al. (2011) for solar metallicity. It is worth noticing that, by including this dependence on the mass-loss rates, we are able to reproduce the observed Humphreys–Davidson transition limit at solar metallicity (Chen et al. 2014b, in preparation). However, to extend this behaviour to different galactic environments, we need to know how the metallicity affects the mass-loss rate near the Eddington limit. This has been thoroughly analysed by Gräfener & Hamann (2008) in a broad metallicity range, $10^{-3}\,Z_\odot \leq Z \leq 2\,Z_\odot$ but only for Wolf–Rayet stars, and by Muijres et al. (2012), who investigated the dependence of mass-loss rate on the CNO abundances. The analysis of Gräfener & Hamann (2008) shows that the dependence of the mass-loss rate on the metallicity is also a strong function of Γ. While at low values of Γ the mass-loss rate obeys the relation $\dot{M} \propto (Z/Z_\odot)^{0.85}\,M_\odot\,{\rm yr}^{-1}$, at increasing Γ the metallicity dependence becomes weaker, and it disappears as Γ approaches 1. In the absence of a more comprehensive analysis of the dependence of the mass-loss rates on the surface metallicity and Γ, we have adopted the results of Gräfener & Hamann (2008). In brief, we assume that the mass-loss rates scale with the metallicity as

$$\dot{M} \propto (Z/Z_\odot)^{\alpha}, \qquad (2)$$

with the coefficient α determined from a fit to the published relationships by Gräfener & Hamann (2008):

$$\begin{aligned} \alpha &= 0.85 && (\Gamma < 2/3) \\ \alpha &= 2.45 - 2.4 \times \Gamma && (2/3 \leq \Gamma \leq 1) \end{aligned} \qquad (3)$$

In summary, our algorithm for the mass-loss rates in different evolutionary phases and metallicities is the following. Besides the already specified mass-loss rate formulation $R_{\rm V01}$, we compute also the dependence on Γ, using the tables provided by Vink et al. (2011), R_{Γ}. However, we scale R_{Γ} with the metallicity, using equations (2) and (3).

During the phases for blue supergiants, luminous blue variables and red supergiants, we adopt the maximum of $R_{\rm V01}$, $R_{\rm dJ}$ and R_{Γ}. When the stars enter the Wolf–Rayet phase, which we assume to begin when the surface hydrogen fraction falls below $X = 0.3$ and the effective temperature $T_{\rm eff} > 30\,000$ K, we consider also the Nugis & Lamers (2000) formulation and we adopt the maximum $\dot{M}$ of $R_{\rm V01}$, $R_{\rm dJ}$, R_{Γ} and $R_{\rm NL}$, after scaling each rate with the metallicity using the appropriate scaling law. In this way, we also obtain a smooth transition between the mass-loss rates in the different evolutionary phases.

2.4 The evolution across the HR diagram

In Figs 1 and 2 we plot the HR diagrams of our new evolutionary tracks of massive stars together with those of intermediate mass stars, for two different values of the chemical composition, $Z = 0.001$ and $Z = 0.004$. In each figure, the three panels from top to bottom, are for three different values of the envelope overshooting, EO = $0.7H_{\rm P}$ (the standard *PARSEC* V1.1 value), EO = $2H_{\rm P}$ and EO = $4H_{\rm P}$, respectively. For each evolutionary track, the central hydrogen-burning phase is coloured in blue, the central helium-burning phase in green and the contraction phases in red while, for clarity, the pre-main-sequence phase is not reproduced.

The black lines at the highest luminosities show the Humphreys & Davidson (1979) limit. This limit marks the region of the HR diagram where, at near solar metallicity, there are no observed supergiant stars. The lack of supergiant stars in this region is interpreted as a signature of the effects of enhanced mass-loss rates when a star enter this region. This interpretation is supported by the presence, around this limit, of luminous blue variable stars, which are known to be characterized by high mass-loss rates. Indeed, the Humphreys & Davidson (1979) limit is well reproduced by our new models at near-solar metallicity, due to the boosting of mass-loss rates near the Eddington limit (Chen et al. 2014b, in preparation). However, at the metallicities investigated in this paper, $Z = 0.001$ and $Z = 0.004$, the boosting is mitigated by the reduction factor introduced by equations (2) and (3). At $Z = 0.001$, the upper main sequence widens significantly and the more massive stars, because of their very large convective cores, evolve in the forbidden region even during the H-burning phase. They also ignite and burn central helium as red supergiant stars. Notice that the most massive stars begin the main sequence already within the forbidden region. At larger metallicity, $Z = 0.004$, the widening of the upper main sequence begins at lower luminosity because of the larger opacities of the external layers but, at the same time, the effects of the mass-loss enhancement near the Eddington limit are more relevant. For both metallicities, in the most massive stars the mass-loss rates are high enough to peel off a significant fraction of the hydrogen-rich envelope and the stars exhaust central hydrogen near the Humphreys & Davidson (1979) limit. Nevertheless, after central He ignition, the stars still move towards the red supergiant phase, until mass loss peels off the entire envelope and the stars evolve back, towards the Wolf–Rayet phase. This effect is more evident at higher metallicity.

At lower luminosities the intensity of mass-loss is lower and it can no longer affect the surface evolution of the stars. There is an intermediate region in the HR diagram where stars ignite helium

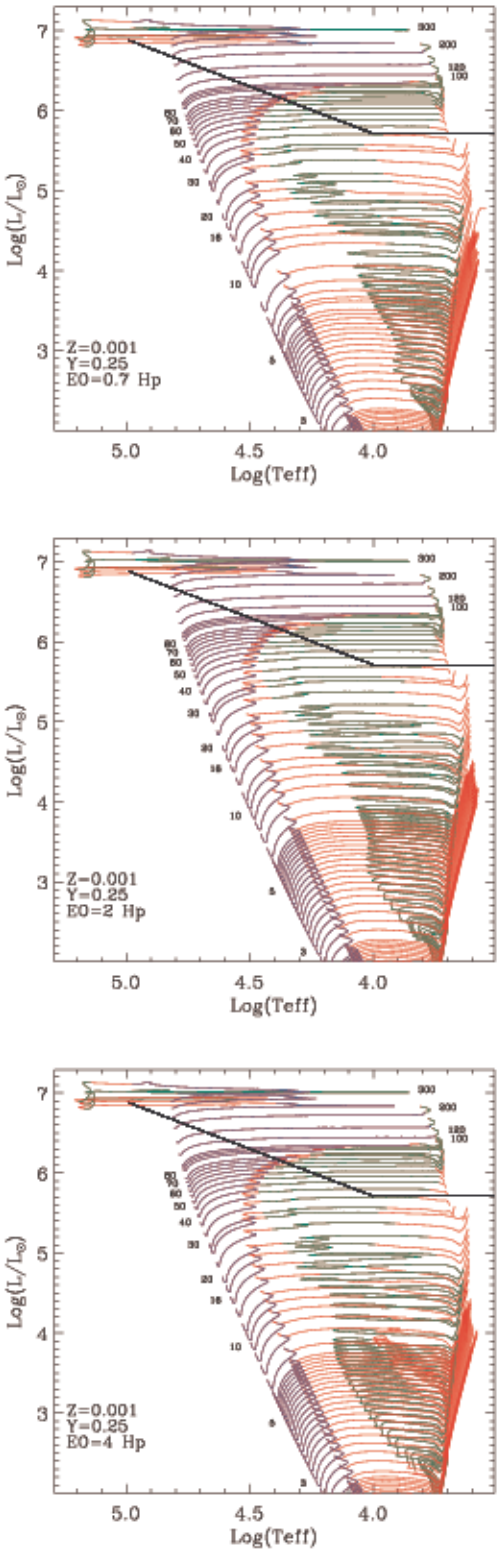

Figure 1. New *PARSEC* evolutionary tracks of massive stars together with already published tracks of intermediate mass stars for $Z = 0.001$. The three panels refer to the different values of envelope overshooting (EO), as indicated in the labels. The black lines indicate the observed Humphreys & Davidson (1979) transition limit at solar metallicity. As in the previous figure, the mass range shown is between about 3 and 350 $M_{\odot}$. Blue, green and red highlight the central H-burning, central He-burning and expansion/contraction phases, respectively. A few tracks are labelled with the initial mass.

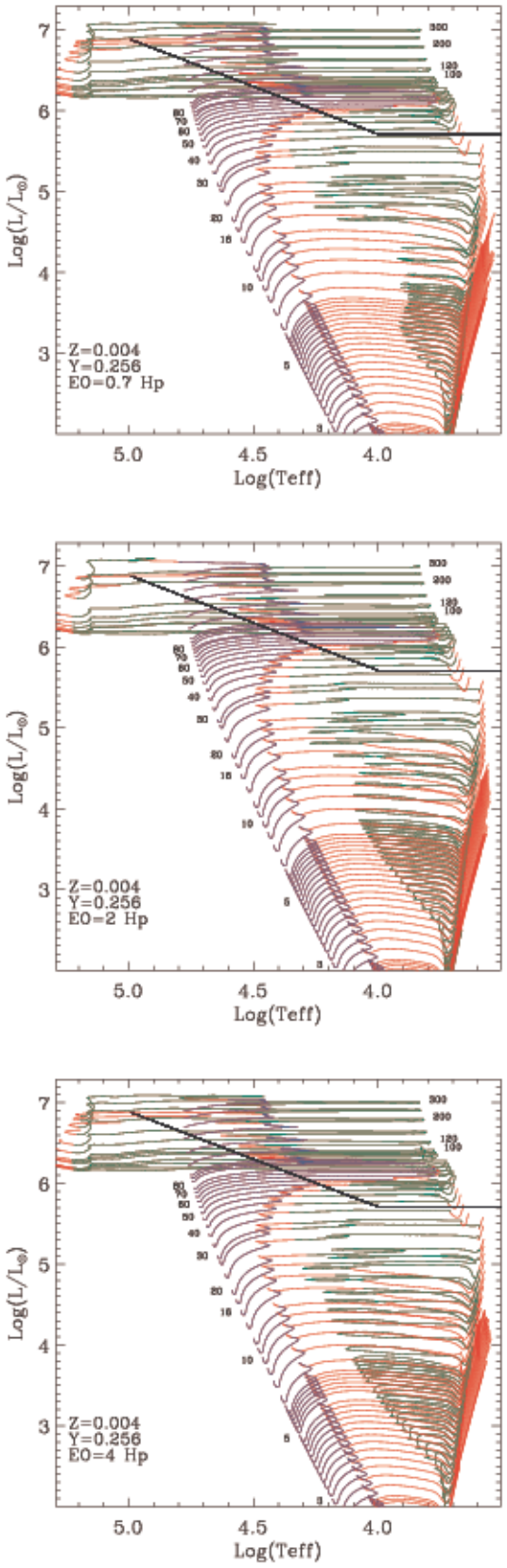

Figure 2. Same as Fig. 1 but for $Z = 0.004$.

burning near the main sequence and then evolve towards the red supergiant phase. At decreasing initial mass, central He ignition shifts towards the red supergiant phase and the path of the stars in the HR diagram becomes similar to that of intermediate mass stars, with the presence of blue loops during the central helium-burning phase. In general, the blue loops are wider for higher initial mass, indicating the existence of a bifurcation in the central helium-burning sequences that begins at intermediate mass stars and persists up to the massive stars. Together with the main sequence, these sequences are the most distinct features in the CMDs of star-forming galaxies and constitute the anchors of any study based on the simulated CMD. On simple grounds they can be explained by considering equilibrium structures made by a helium core and a non-negligible outer hydrogen-rich envelope. In the HR diagram these equilibrium structures are expected to lie between the main sequence and the Hayashi line (Lauterborn, Refsdal & Weigert 1971). They lie near the main sequence when the helium core is negligible, and near the Hayashi line when the virial temperature of the helium core, $\propto \Phi = M_C/R_C$ with M_C and R_C being the mass and radius of the helium core, is larger than a critical threshold. The latter depends on the mass of the star, the chemical composition, some reaction rates and possibly other input physics such as internal mixing, rendering the morphology of the loops quite dependent on several details of stellar evolution (Iben 1966; Brunish & Becker 1990; Xu & Li 2004; Weiss et al. 2005; Halabi et al. 2012). Such complex dependence makes the theoretical predictions quite difficult, especially at increasing metallicity. For example at $Z = 0.001$ with canonical envelope overshooting (top panel of Fig. 1), at increasing luminosity the loops become initially quite extended but then their extent decreases and thereafter increases again. This behaviour is even more marked at $Z = 0.004$ (upper panel of Fig. 2). The loops initially become more extended at increasing mass, but above $M = 6.4\,M_\odot$ their extent decreases, and they even disappear for $M = 10$ and $11\,M_\odot$. Above these masses, they fully develop again until the beginning of central He burning shifts in the yellow/blue side of the HR diagram.

2.5 Blue loops: the role of envelope overshooting

The reason for the presence or absence of extended blue loops during the central helium-burning phase has been thoroughly investigated in the past. Among the effects that limit the extent or inhibit the appearance of blue loops, the most important one is certainly extended mixing from the core during the hydrogen-burning phase, either due to overshooting (Bertelli et al. 1985) or to differential rotation (Heger & Langer 2000; Georgy et al. 2013). This effect can be understood by considering that it is more difficult for a star with a larger He core to decrease Φ below the critical value needed to begin the loop, because Φ increases with the core mass in a virialized structure, for which the radius increases with a power ($\sim$0.5) of the mass. On the other hand, it is well known that the presence of extended mixing below the bottom of the convective envelope favours the development of an extended loop (Alongi et al. 1991). To clarify this point better, we show in Fig. 3 the evolution of the internal structure during the central helium-burning phase, of a model with $M = 11\,M_\odot$ and $Z = 0.004$, computed with canonical core overshooting and three different values of the envelope overshooting: EO $= 0.7H_P$ (*PARSEC* V1.1), EO $= 2H_P$ and EO $= 4H_P$. The models begin helium burning with the same internal structure, apart from the larger inward penetration of the envelope convection due to the different efficiency of the overshooting during the first dredge-up episode, which changes the location of the

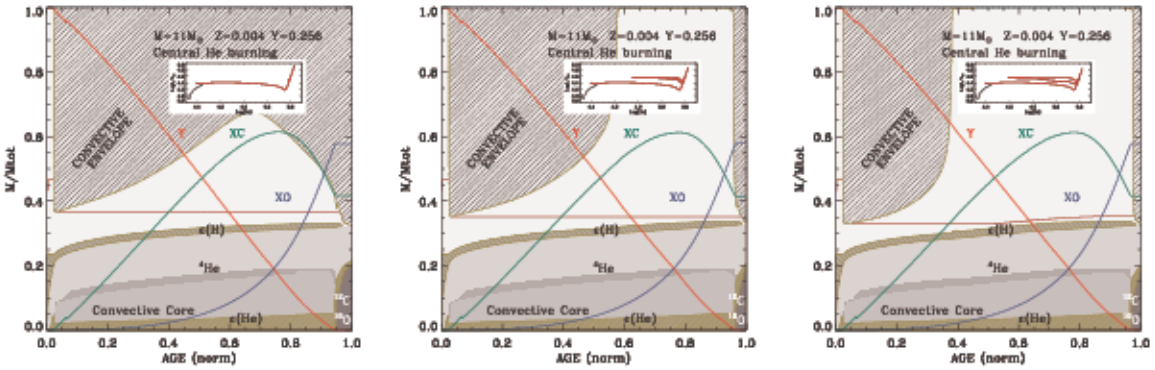

Figure 3. Kippenhahn diagrams of central helium-burning model stars for $M = 11$ M$_\odot$ and $Z = 0.004$ computed with different envelope overshooting, EO $= 0.7H_P$, EO $= 2H_P$ and EO $= 4H_P$, from left to right. The insets show the corresponding evolutionary tracks in the HR diagram.

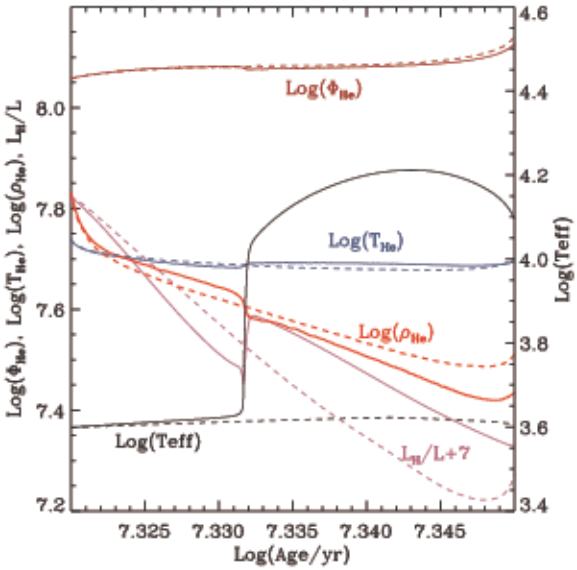

Figure 4. Evolution of the effective temperature, the H-shell luminosity and other quantities evaluated at the border of the He core, for the models of Fig. 3 with envelope overshooting values EO $= 0.7H_P$ (dashed lines) and EO $= 4H_P$ (solid lines). See text for more details.

hydrogen/helium discontinuity (indicated in the figure by the brown horizontal line at $M/M_{tot} \sim 0.35$). Comparing the three models, the only noticeable internal difference is the size of the mass pocket between the H-burning shell and the H–He discontinuity left by the first dredge-up episode. Only the models with enhanced envelope overshooting (EO $= 2H_P$ and EO $= 4H_P$) perform an extended blue loop. The loop begins when the central hydrogen shell approaches the H–He discontinuity, in a way that reminds us of what happens to a red giant star when its internal hydrogen shell reaches the hydrogen discontinuity. Because of the high temperature dependence of the CNO reaction rates, when a discontinuity in the hydrogen profile is encountered, the structure readjusts on a thermal timescale towards a slightly lower luminosity and a higher effective temperature. Afterwards, the star continues climbing the RGB on the nuclear timescale, giving rise to the well-known bump in the luminosity function. What happens in the interiors of the different models of $M = 11$ M$_\odot$ can be seen in Fig. 4, where we compare several quantities as a function of the evolutionary time during central helium burning. The dashed lines in the figure refer to the standard *PARSEC* V1.1 model (EO $= 0.7H_P$) while the solid lines to the model with EO $= 4H_P$ (see also Fig. 3). While helium burning proceeds, the temperature and the density at the border of the He core continuously decrease. Once the H-burning shell approaches the H discontinuity (brown horizontal line in Fig. 3) in the model with large EO, the density decreases and the temperature increases on a thermal timescale. At the same time, the H luminosity increases from 50 to 60 per cent while the star shifts towards the main sequence, in the blue loop. Notice that Φ has a deep during this transition.

With the models for $M = 10$ and 11 M$_\odot$ for $Z = 0.004$, with canonical core and envelope overshooting (*PARSEC* V1.1), we also analyse the importance of changing other parameters, such as the mixing length, the $^{12}C(\alpha, \gamma)^{16}O$ reaction rate (Iben 1966; Bertelli et al. 1985; Brunish & Becker 1990) and the $^{14}N(p, \gamma)^{15}O$ reaction rate (Xu & Li 2004; Weiss et al. 2005; Halabi et al. 2012), because these parameters are known to affect the extent of the loops. We find that by modifying these parameters within a suitable range the above models are not able to perform extended blue loops in the HR diagram. We thus conclude that the most critical parameter for the morphology of the He blue loop is the size of the mass pocket between the advancing H-burning shell and the H discontinuity left by the previous first convective dredge-up (Alongi et al. 1991; Godart et al. 2013). The earlier the shell approaches this discontinuity, the earlier the loop begins and the larger is its extent.

For this reason and in view of the comparison of the new models with the observations that will be performed in the next sections, we compute additional sets of models with an increased amount of envelope overshooting, i.e. with EO $= 2H_P$ and EO $= 4H_P$. The stellar evolutionary tracks with increased envelope overshooting are shown in the middle and lower panels of Figs 1 and 2 for $Z = 0.001$ and $Z = 0.004$, respectively. As expected, after including a larger mixing at the base of the convective envelope, the blue loops become more extended, though at the lower metallicity the effect is not large. In this case, only by assuming a large mixing scale (EO $= 4H_P$) does the effect becomes significant. It is worth noticing that, though large, values of EO between $2H_P$ and $4H_P$ are not uncommon. For example, they are used to enhance the efficiency of the carbon dredge-up during the thermally pulsing asymptotic giant branch phase (Kamath, Karakas & Wood 2012).

3 DATA

3.1 Photometric data

To compare our models with observations, we use photometry from Bianchi et al. (2012b)'s *HST* treasury survey HST-GO-11079, which imaged star-forming regions in six Local Group dwarf galaxies,

Phoenix, Pegasus, Sextans A, Sextans B, WLM and NGC 6822, and in M31 and M33. Multi-band imaging with WFPC2 includes six filters from the far-UV to near-IR: F170W, F255W, F336W, F439W, F555W and F814W.[4] The Bianchi et al. (2012b) survey focused on the massive stars in these galaxies, therefore the exposures were tuned to provide complete filter coverage with high signal-to-noise (S/N) for the hottest stars, while cooler stars have progressively lower S/N in the UV filters. We refer the reader to Bianchi et al. (2012b) for details of the data reduction and photometric quality; for the purpose of this work it is sufficient to recall that incompleteness reaches 20 per cent at mag = 21.0, 22.8, 22.9 and 22.0 in F336W, F439W, F555W and F814W, respectively.

After careful examination of the CMDs, we conclude that the three best galaxies suitable for the analysis of their star formation history (SFH) to check the performance of the new *PARSEC* V1.1 models of massive stars at low metallicity are WLM, NGC 6822 and Sextans A. The other three galaxies, Phoenix, Pegasus and Sextans B, are less populated by massive stars and therefore less suitable for our purpose. Furthermore, deeper photometry in the F555W and F814W filters is available for Sextans A (HST-GO-10915, Dalcanton et al. 2009), which we use for comparison with simulated CMDs. The CMDs of Sextans A, WLM and NGC 6822 are shown in the upper panels of Figs 8, 9 and 10, respectively.

3.2 Metallicity of the sample galaxies

To select the appropriate metallicity of the models, we examined the literature for existing measurements of abundances in our sample galaxies.

3.2.1 *The metallicity of Sextans A*

An oxygen nebular abundance of $12 + \log(\mathrm{O/H}) = 7.49$ for Sextans A, was obtained by Skillman, Kennicutt & Hodge (1989) by optical spectrophotometry of H II regions. Comparing synthetic and observed CMDs, Dolphin et al. (2003b) obtained a mean metallicity of $[\mathrm{M/H}] = -1.45 \pm 0.2$ throughout the measured history of the galaxy. Analysis of three isolated A-type supergiants by Kaufer et al. (2004) yielded a present-day stellar abundance of the α element Mg as $\langle[\alpha(\mathrm{Mg\,I})/\mathrm{H}]\rangle = -1.09 \pm 0.02$. Finally, Kniazev et al. (2005) presented spectroscopic observations of three H II regions and a planetary nebula in Sextans A. They derived an average oxygen abundance of $12 + \log(\mathrm{O/H}) = 7.54 \pm 0.06$ in the H II regions, which agrees well with data from Kaufer et al. (2004). However, the oxygen abundance of the planetary nebula is significantly higher, $12 + \log(\mathrm{O/H}) = 8.02 \pm 0.05$, and it is explained as self-pollution by the planetary nebula progenitor. Adopting the oxygen solar abundance of $12 + \log(\mathrm{O/H}) = 8.66$ based on the 3D model (Asplund et al. 2004) and the corresponding total metallicity ($Z \sim 0.014$), we obtain for the young populations of Sextans A a metallicity of $Z \sim 0.001$. For this galaxy we will use *PARSEC* V1.1 models with $Z = 0.001$.

3.2.2 *The metallicity of WLM*

For WLM, Skillman, Terlevich & Melnick (1989) and Hodge & Miller (1995) measured oxygen nebular abundances of $12 + \log(\mathrm{O/H}) = 7.74$ and 7.77, respectively. Venn et al. (2003) found a significant discrepancy between nebular abundance ($[\mathrm{O/H}] = -0.89$) and stellar abundance ($[\mathrm{O/H}] = -0.21 \pm 0.10$). From a study of nine H II regions, Lee, Skillman & Venn (2005) obtained a mean nebular oxygen abundance of $12 + \log(\mathrm{O/H}) = 7.83 \pm 0.06$, corresponding to $[\mathrm{O/H}] = -0.83$ when adopting the solar oxygen abundance of $12 + \log(\mathrm{O/H}) = 8.66$ (Asplund et al. 2004). This is in excellent agreement with the measurement of Bresolin et al. (2006), who carried out a quantitative analysis of three early B supergiants and derived an average of $12 + \log(\mathrm{O/H}) = 7.83 \pm 0.12$. Finally, Urbaneja et al. (2008) obtained a weighted mean metallicity $[\mathrm{Z/H}] = -0.87 \pm 0.06$ for several B and A supergiants, a result consistent with the previous measurements. The metallicity of the young populations is thus $[\mathrm{O/H}] \sim -0.9$, which corresponds to $Z \sim 0.0017$. Even though this value is larger than that of Sextans A, in the following analysis we will make use of the same models adopted for Sextans A, so that the models with $Z = 0.001$ are compared with two bracketing samples of observational data.

3.2.3 *The metallicity of NGC 6822*

The nebular abundance of NGC 6822 was found to be $12 + \log(\mathrm{O/H}) = 8.25 \pm 0.07$ from a spectroscopic analysis of seven H II regions (Pagel, Edmunds & Smith 1980). This result is supported by Richer & McCall (1995), who observed two planetary nebulae, and deduced oxygen abundances $12 + \log(\mathrm{O/H}) = 8.10$ and 8.01, respectively. From a spectral study of A-type supergiants, Venn et al. (2001) derived an average oxygen abundance of $12 + \log(\mathrm{O/H}) = 8.36 \pm 0.19$ and $[\mathrm{Fe/H}] = -0.49 \pm 0.22$ for the young star population, suggesting also the presence of a gradient in [O/H]. Tolstoy et al. (2001) measured the Ca II triplet in RGB stars and estimated the mean metallicity of the old stars to be $[\mathrm{Fe/H}] = -1 \pm 0.5$, with values of individual stars ranging from -2.0 to -0.5. This average value agrees well with Davidge (2003), who obtained the same value from the slope of the RGB. Using the ratio between C type and M type asymptotic giant branch stars, Cioni & Habing (2005) derived a spread of the metallicity $\Delta[\mathrm{Fe/H}] = 1.56$ dex, and Kang et al. (2006) found $\Delta[\mathrm{Fe/H}] = 0.07$–$0.09$ dex in the bar. Moreover, Sibbons et al. (2012) obtained $[\mathrm{Fe/H}] = -1.29 \pm 0.07$. The metallicity of NGC 6822 is definitely higher than that of Sextans A and WLM and therefore we need to use higher metallicity models to analyse its CMD. To favour models with extended blue loops and thus to avoid any possible problem due to the adoption of a too high metallicity, we will adopt the lowest value compatible with observations of the young populations. Both the lowest values of [O/H] by Pagel et al. (1980) and Venn et al. (2001) are compatible with $Z \sim 0.0045$, again using $12 + \log(\mathrm{O/H}) = 8.66$ and $Z = 0.014$ for the Sun. The simulation of NGC 6822 will thus be performed using models with $Z = 0.004$.

3.3 Contamination by foreground stars

The contamination of the observed CMDs by foreground Galactic stars was estimated using the TRILEGAL code (Girardi et al. 2005) via its web-based interface.[5] The four Galactic components taken into account in TRILEGAL are the thin disc, the thick disc, the halo and the bulge, for which we assume the default values of the geometrical and constitutive parameters [star formation rate (SFR), metallicity, initial mass function (IMF) and extinction], as specified in the web interface and in the references quoted there. In particular,

[4] http://dolomiti.pha.jhu.edu/LocalGroup/

[5] http://stev.oapd.inaf.it/cgi-bin/trilegal

the IMF is assumed to be represented by a log-normal function (Chabrier 2001) for all the components. Extinction is applied to individual stars in the Galaxy, assuming a dust disc described by a double-exponential decay,

$$A_V \propto \exp(-|z|/h_{z,\mathrm{dust}}) \times \exp(-R/h_{R,\mathrm{dust}}). \quad (4)$$

with default values of scale height $h_{z,\mathrm{dust}} = 110$ pc, scale length $h_{R,\mathrm{dust}} = 100$ kpc and total absorption at infinity $A_V(\infty) = 0.0378$ mag. To calculate the absorption in each *HST* filter, we use the Galactic extinction curve with $R_V = 3.1$ (Cardelli, Clayton & Mathis 1989). We also take into account the effects of unresolved binary systems, assuming the default values, i.e. a fraction of 30 per cent and mass ratios uniformly distributed between 0.7 and 1. We performed TRILEGAL simulations in the direction of the three galaxies used in our analysis, and scaled the resulting number of stars to the areas covered by the *HST* survey, given in table 1 of Bianchi et al. (2012b). We extended the TRILEGAL MW model calculations to a limiting magnitude of 25 mag in F439W. The TRILEGAL simulations indicate that only for NGC 6822 is there significant contamination, as expected because of its low Galactic latitude. Fig. 7 shows the simulated MW foreground stars on the CMD of NGC 6822. The contamination has the shape of a plume around $m_{F439W} - m_{F555W} \sim 1.0$, which occupies the region between the blue and the red sequences of NGC 6822, likely true members of the galaxy. To quantify the contamination, we counted the simulated stars that fall within the box $0.5 < m_{F439W} - m_{F555W} < 1.4$ and $18 < m_{F439W} < 22.5$, in the CMD. In this region we count 336 stars in the observed CMD while the simulation predicts there would be 93 stars in the thin disc (blue crosses), 118 in the thick disc (green crosses), 59 in the halo (red crosses) and four bulge stars (cyan crosses). In total, we find that there could be 178 possible MW stars in the selected box, indicating that, for NGC 6822, the MW contamination above $m_{F439W} - m_{F555W} > 0.5$ is severe and must be taken into account in the comparison of the simulated and observed CMDs (Section 4 below).

For Sextans A and WLM, the contamination is negligible.

4 SIMULATED COLOUR MAGNITUDE DIAGRAMS

To obtain the simulations of the observed CMDs, we modified the code that computes the *PARSEC* isochrones, allowing the selection of a distribution of stars with suitable SFH and IMF.

Since our analysis is limited to the youngest stars, we do not take into account an age metallicity relation but instead we fix the abundance to the most likely value of the burst, taken from the literature as discussed in Section 3. The SFR is specified as a simple function of time (SFH). For the IMF, we assume a simple two-power-laws representation, a Kennicutt IMF (Kennicutt 1998), however, with parametrized exponent above 1 $M_\odot$. The SFH and, to a lesser degree, the shape of the IMF are tuned to reproduce the stellar number counts as described below. To convert luminosity, effective temperature and gravity into magnitude and colours, we adopt the bolometric correction tables as in Marigo et al. (2008). These tables are obtained by convolving large libraries of stellar spectra with the filters' transmission curves being considered, as described in Girardi et al. (2002). In the ranges of effective temperature, surface gravity and metallicity relevant to this work, we use the spectra derived from the ATLAS9 model atmospheres (Castelli & Kurucz 2003), which are well calibrated against observations. In the more advanced phases (red supergiants and Wolf–Rayet stars) and for the highest masses, where the effects of mass loss may be significant, some discrepancies may somewhat affect the transition to different spectral libraries, but these differences do not alter our results because these stars are only a minority in the analysed CMDs.

To avoid simulating unnecessarily large numbers of stars, we define a suitable absolute limiting magnitude by taking into account the distance modulus of the galaxies and the faintest magnitude at which the incompleteness reaches 20 per cent in each filter, which is ≈23 mag for F439W and F555W (Bianchi et al. 2012b). For the simulations of WLM and NGC 6822, we thus select a limiting apparent magnitude of F439W = 23.5 mag. We adopt the same magnitude limit, F555W = 23.5 mag, also for Sextans A, to avoid the inclusion of less massive stars in the simulation, even if the same incompleteness level is reached at fainter magnitudes in the Dalcanton et al. (2009) data.

The outcome of this procedure is a clean absolute CMD that must be translated into the observational plane by adopting the proper distance modulus and assigning suitable values of error and extinction to each star, as described below. With this procedure we generate, for each form of SFH and IMF, simulated catalogues containing many more stars than those in the observed CMDs. The simulated CMDs are thus drawn from subsets of these large catalogues, and this procedure is repeated 100 times to obtain the best-fitting luminosity function and its standard deviation, for the selected input parameters.

4.1 Simulated errors

The simulated photometric errors have been derived from the distribution of the observational errors as a function of the apparent magnitude (Dalcanton et al. 2009; Bianchi et al. 2012b), as follows. For WLM and NGC 6822, we select sources with HSTphot type = 1 and |sharpness| < 0.3 and we plot errors versus apparent magnitude. These figures are similar to those shown in Bianchi et al. (2012b) and are not reproduced here. To estimate individual errors for the simulated stars in a given filter, we re-bin the error distribution in 0.1 magnitude bins and, within each magnitude bin, we evaluate the median error. Then, the error assigned to each model star of a given apparent magnitude is randomly drawn from a Gaussian distribution with a standard deviation derived from the median value corresponding to its magnitude. An example of the simulated error for the F439W filter for WLM is shown in Fig. 5. For Sextans A, the errors are determined in the same way, but using the data from Dalcanton et al. (2009).

4.2 Accounting for extinction

In the analysis of the CMDs of stellar systems, extinction is generally treated as a constant free parameter that must be derived from a fitting procedure. In this respect, a key feature of this investigation is that we may exploit the information carried by the multi-band photometric coverage of the observations because our galaxies were observed in six *HST* bands by Bianchi et al. (2012b). For many of the observed stars, the photometry spectral energy distributions (SEDs) can be modelled to obtain extinction, effective temperature and bolometric luminosity at once. We use such results to define the attenuation on a star-by-star basis, in a statistical way.

We use extinction results from Bianchi et al. (2012b)'s SED fitting of the multi-band *HST* photometry with theoretical spectral libraries of different metallicities, $Z = 0.0002$, $Z = 0.002$ and $Z = 0.02$, and different extinction curves, average MW with $R_v = 3.1$ (Cardelli et al. 1989), Large Magellanic Cloud 2 (LMC2) (Misselt, Clayton & Gordon 1999) or Small Magellanic Cloud (SMC) (Gordon &

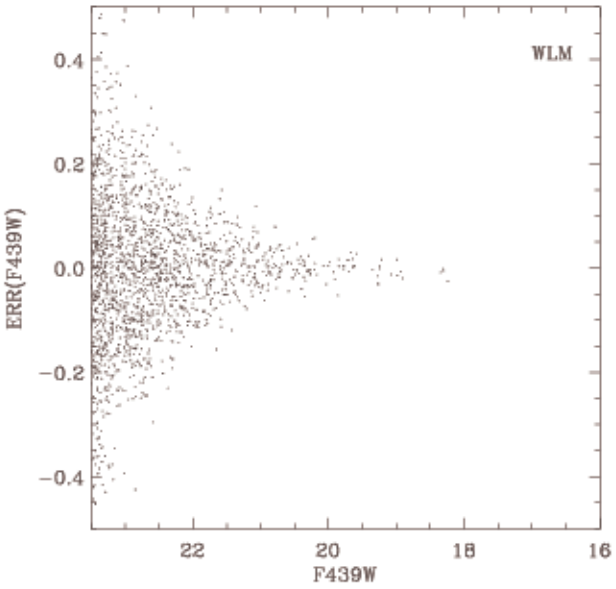

Figure 5. Simulated photometric errors as a function of the apparent magnitude for the F439W filter for WLM stars.

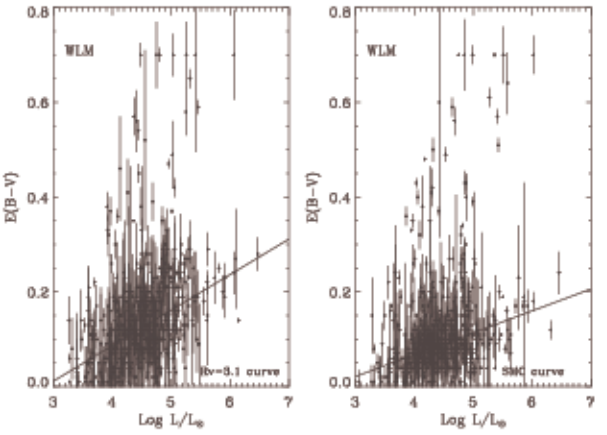

Figure 6. Reddening of WLM stars, derived from multi-band SED fitting using the Galactic (left panel) or the SMC (right panel) extinction curves.

Clayton 1998). We restricted this analysis to sources with photometric accuracy better than 0.25, 0.20, 0.25, 0.10 or 0.10, for the filters F170W, F225W, F336W, F439W and F555W respectively, and applied no error cut-off for F814W. Such sample restriction to stars detected in at least five filters, with small photometric errors in the optical bands, ensures that enough measurements are available for each star for deriving concurrently two free parameters ($T_{\rm eff}$ and $E(B-V)$), and biases the analysis sample towards the hottest, most luminous stars, because we require detection even for the far-UV filter. Results from this survey and similar ones show that the hottest stars are usually found in regions of high interstellar extinction (see e.g. Bianchi et al. 2012b, fig. 12), as we shall discuss later. The resulting extinction depends significantly on the adopted attenuation curve (see also Bianchi et al. 2012b) but much less on the adopted metallicity of the theoretical spectra.

As an example, we show in Fig. 6 the extinction derived for the stars in WLM by Bianchi et al. (2012b). The two panels show two different cases obtained with the same spectral library, $Z = 0.002$, and two different extinction laws, the Galactic one ($R_V = 3.1$) in the left panel and the SMC one, in the right panel. For each star, $E(B-V)$ is plotted against the stellar bolometric luminosity, which is also derived from the best fit of the observed SED, assuming the distance of the galaxy. The vertical error bars depict the uncertainties, derived in the SED-fitting process. In addition to the formal uncertainties, there may be a slight bias due to poor calibration of the WFPC2 UV filters (Charge Transfer Efficiency [CTE] corrections) as discussed by Bianchi et al. (2012a). Fig. 6 shows a trend of increasing $E(B-V)$ at increasing luminosity. The line shown in the figure is a simple best fit to the data obtained after selecting only those with a relative error $\leq$0.2 and excluding the outliers (using the LADFIT IDL procedure). The lines in the panels show a clear positive slope with the stellar intrinsic luminosity. The slope obtained with the Galactic extinction law (left panel) is about 50 per cent larger than that obtained with the SMC extinction law. We also observe a significant dispersion at all luminosities and, in general, the more luminous stars have smaller uncertainties.

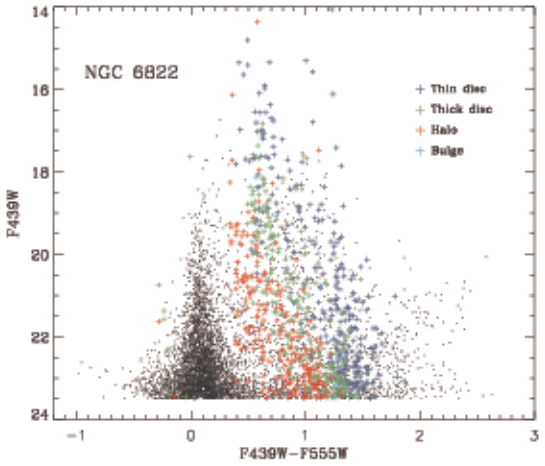

Figure 7. Estimated MW contamination in the CMD of NGC 6822. Black dots are the observed stars while coloured dots are the predicted contamination by the four Galactic components as indicated in the labels.

Of course the derived extinction includes the contribution arising from the MW, which should be almost constant in a given field though we notice that, at the lower luminosities, there are values that are even less than the contribution of the Galaxy. However, within the uncertainties, they are compatible with the foreground value, which is significant only for NGC 6822. Instead we suppose that the dependence of the additional attenuation with the intrinsic luminosity is a clear signature that the internal extinction is age-selective (Silva et al. 1998). In this case, the trend arises because younger stars are embedded in a more opaque interstellar medium, independently of their mass and luminosity, while older stars, which are generally less massive and of lower luminosity, may be less attenuated. Another noticeable feature is that in the higher luminosity bins, the errors are small and the observed values indicate that there can be significant star-to-star variation in the extinction. There are also a few stars with small error bars and significantly higher than average extinction. These are generally stars cooler than the main sequence ones and a likely explanation for their large extinction is that they could be affected by dust produced by their own circumstellar envelopes. Since there are only a small number of such stars, they are excluded from the fits shown in Fig. 6, but this point could deserve further investigation because it could be an evidence of pristine dust production in low metallicity galaxies. In summary, there is evidence that in our galaxies extinction may grow with

intrinsic luminosity for the hot stars, and may have a significant star-to-star variation. To account for these effects in the simulated CMD, we randomly distribute the extinction values as a function of the (known) intrinsic luminosity of our model stars, by reproducing the best-fit relation and the observed dispersion with a Gaussian model. This effect introduces a further dispersion in the simulated CMDs, which adds to that of the photometric errors and possibly a tilt in the modelled stellar sequences. Because we modelled the extinction distribution on a sample of hot stars, which are mostly associated with regions of high extinction, we should keep in mind in the following discussion that if cooler stars outside the star-forming regions are included in the catalogue, the model extinction distribution may be overestimated for them; this is not the case for the Bianchi et al. (2012b) survey, which mostly targeted conspicuous star-forming regions.

For Sextans A, we fit the star-to-star attenuation model derived from the multi-band data by Bianchi et al. (2012b), and apply it to the F555W and F814W deeper data by Dalcanton et al. (2009), using the selected extinction law. Since in the considered range of magnitudes the errors are negligible in the Dalcanton et al. (2009) photometry, the variable extinction is practically the only source of star-to-star dispersion in the simulated CMD of Sextans A.

5 RESULTS WITH CANONICAL MODELS

As already anticipated in Section 2, the simulations of the CMDs of the three galaxies are based on stellar evolution models that use different values of the envelope overshooting. We begin by discussing the results obtained by using the standard value adopted in *PARSEC* V1.1, i.e. an envelope overshooting of EO $= 0.7H_P$.

5.1 Sextans A

5.1.1 The colour magnitude diagram

The observed CMD of Sextans A, reproduced in the upper panel of Fig. 8, shows the following noticeable features. There is a well-defined main sequence with stars brighter than F555W $= 23.5$ (our selected magnitude limit) and bluer than F555W $-$ F814W ≤ -0.1. The sequence appears to become broader and redder at brighter magnitudes. This effect is unusual because, in general, the sequence becomes bluer and narrower at brighter magnitudes, due to the smaller photometric errors. A parallel sequence, redder by about 0.2–0.3 mag, is also visible and likely corresponds to the stars that are burning helium in the blue loops. This may not be the case for the brightest stars that, as shown in the HR diagrams, may ignite central helium before reaching the red supergiant phase. A red sequence, starting at F555W $-$ F814W ~ 1, indicates the presence of red giant/supergiant stars in the red phase before the loop. Only a scarce number of stars populate the region between the RHeBS and BHeBS, as expected because of the short crossing timescales of the Hertzsprung gap. The stars found in this gap are likely yellow supergiants, since the MW contamination that mainly affects this region of the CMD is low for this galaxy. The RGB and Asymptotic Giant Branch (AGB) phases of low and intermediate mass make up the sequences at even redder colours (F555W $-$ F814W ≥ 1.2).

For the simulations of Sextans A, we adopt a distance modulus $(m - M)_0 = 25.61$ (Dolphin et al. 2003a). The best simulation obtained with *PARSEC* V1.1 models is shown in the middle panel of Fig. 8. This simulation has been selected from 100 stochastic realizations made with the same parameters, using a merit function based on the differences between the observed and simulated luminosity

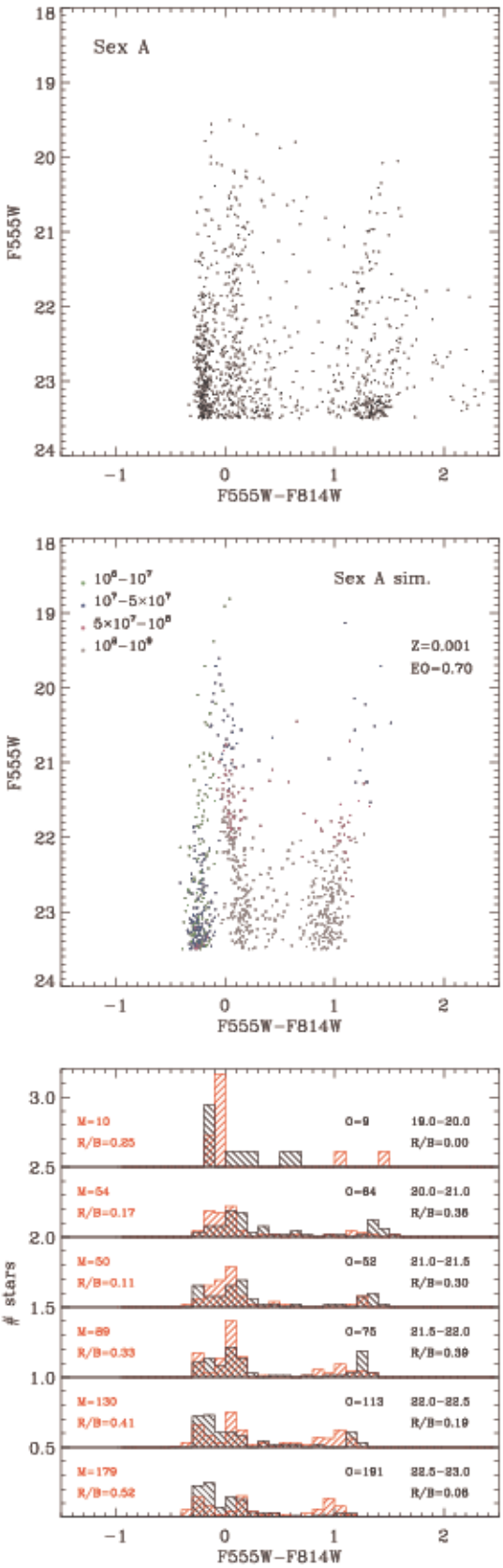

Figure 8. Upper panel: Observed CMD for Sextans A. Middle panel: The best model obtained with *PARSEC* V1.1. Lower panel: Comparison of the observed (black) and modelled (red) colour distributions.

Table 1. Parameters of the CMD simulations of Sextans A.

EO	T_i [yr]	T_f [yr]	τ [yr]	$X_{\rm IMF}$	$\langle$SFR$\rangle$ [$M_\odot$ yr^{-1}]
0.7	1×10^6	1×10^9	-2×10^8	2.35	2.5×10^{-3}
2	1×10^6	1×10^9	-2×10^8	2.35	2.9×10^{-3}
4	1×10^6	1×10^9	-1×10^8	2.35	3.2×10^{-3}

functions. Stars of different ages are shown with different colours in the simulated CMD, as indicated in the corresponding labels. The metallicity adopted for the simulation is $Z = 0.001$. The simulated CMD reproduces qualitatively all the main features of the observed diagram, except for the stars redder than F555W − F814W $\geq$ 1.2 and the sequences that depart from there. This is because we impose a cut-off in the simulation at masses below 1.9 $M_\odot$, since we are interested in the recent SFH of the galaxy. For the same reason we discarded from the analysis below all stars in the observed diagram redder than the line F555W − F814W = (31.2 − F555W)/7, which should correspond to the old population.

5.1.2 *The star formation rate*

Since our simulated CMD catalogue is constructed by imposing a total number of living stars brighter than a given threshold luminosity, a few steps are needed to derive the normalization of the SFR that corresponds to the parameters given in Table 1. In particular we have to take into account that our model catalogue is a superset of the observed CMD, to which it should be matched. So, we first need to obtain the SFR normalization of the parent catalogue and then scale this normalization to the number of stars in the observed CMD. For the first step, we selected a small mass interval for which the stellar evolutionary times are larger than the oldest age of our simulation. Since all such stars are still alive, they must all be in the catalogue and they can be easily counted. On the other hand, their number must correspond to the double integral, over the full time interval and the selected mass interval, of the product of the SFR and the IMF. From the comparison between the counted stars and the analytical result of the double integral, we derive the normalization of the model SFR used to generate the large catalogue. To obtain the real SFR from the observed CMD, we simply scale the model SFR by imposing that the model contains the same number of stars as the observed CMD, in the magnitude range between 23 and 21.5. We use this magnitude interval to limit the stochastic effects introduced by the brightest stars. Nevertheless, since the normalization is made after the simulated magnitudes have been assigned attenuation and errors, the SFR so derived may slightly change between different models, even if the underlying parameters are the same. It is worth noting that the normalization obtained in this way may also be affected by all those effects that may modify the luminosity function in a given pass-band. One such effect, as we will see, is the variation of the lifetime of stars in the blue and red sides of the loops. This effect may change the number of stars in the magnitude bins and so the resulting luminosity function. Another possible effect is that of the unresolved binary stars (even if not physical), which artificially increase the number of stars in the brighter magnitude bins. In this respect, *HST*/WFPC2's resolution (0.1 arcsec spatial scale, i.e. less than half a parsec in WLM and Sextans A, and about one-fourth of a parsec projected on the sky, at the distance of NGC 6822) offers a critical advantage with respect to ground-based observations with typical seeing of $\gtrsim$1 arcsec. Quantification of the gain afforded by *HST* imaging in resolving individual stars in these galaxies can be seen, for example, in fig. 3 of Bianchi et al. (2012b). This is particularly relevant for studies of hot stars, which are found in crowded regions because of their young age, the OB associations having not yet dissolved. The very bright stars are rare, but at B and V magnitudes fainter than ≈20, the effect of unresolved stars in ground-based catalogues and the gain from *HST* become very significant. We finally note that for random superposition (along the line of sight) the combined photometry of two likely different types of stars will result in an SED hard to fit with a single star, and the source may be discarded from the analysis with quality cuts.

We find that the SFR increases towards recent times ($\tau < 0$, Table 1) with a characteristic timescale $|\tau| = 2 \times 10^8$ yr. The average SFR in the last 100 Myr is 2.5×10^{-3} $M_\odot$ yr^{-1}, as indicated in Table 1. The maximum mass obtained from the simulation is $M \sim 80$ $M_\odot$. However, with F555W $\sim$ 20.5 mag, this is not the brightest star, which instead is an evolved star with $M \sim 30$ $M_\odot$ and F555W $\sim$ 18.8 mag.

5.1.3 *The colour distribution*

To make the comparison between the observed and simulated CMDs more quantitative, we plot in the lower panel of Fig. 8 the colour distribution of the stars in different bins of F555W magnitude: 19–20, 20–21, 21–21.5, 21.5–22, 22–22.5 and 22.5–23. The black histograms refer to the observed CMDs while the red histograms are for the simulated CMDs. On the right side of each histogram, we show the corresponding magnitude interval, the number of stars observed in the interval (O) and the observed ratio (R/B) of stars redder and bluer than a given threshold colour. On the left side of the histogram, we show the same quantities, number of stars and number ratios (M and R/B), as predicted by the simulations. For Sextans A, we adopted a threshold value of F555W − F814W = 0.6 and, as already specified, we did not consider stars redder than the line F555W − F814W = (31.2 − F555W)/7, which are more likely to belong to older populations.

The colours and in particular the width of the simulated main sequence match fairly well those of the observed one, in all the magnitude bins. Two points are worth discussing. First we note that, since we are using a single metallicity, the observed width of the main sequence should be ascribed mainly to photometric errors, because the intrinsic width at 22 mag is δ(F555W − F814W)$_0 \lesssim 0.07$ mag. But the photometric errors of the observations are very small at these magnitudes. Second, the simulated main sequence is almost vertical in the diagram while, as already said, we would expect this sequence to be inclined towards bluer colours at brighter magnitudes. Both effects are due to the extinction. The extinction was evaluated for individual stars from simultaneous fits for [$T_{\rm eff}$, $E(B-V)$] of multi-band photometry (Bianchi et al. 2012b) using suitably attenuated spectral models. As discussed in Section 4.2, Bianchi et al. (2012b) find that $E(B-V)$, besides showing a significant dispersion, is higher for the hot young stars. The dispersion in the attenuation is intrinsic and due to region-to-region variation. Instead, its rise with luminosity is likely caused by the following bias. All stars are born in a region of relatively higher attenuation and as time elapses, the parent clouds dissolve and the attenuation decreases (Silva et al. 1998). It is well known that the emission lines (signature of young massive stars) in starbursts show an attenuation that is about twice that of the optical continuum (mostly from older, lower mass stars) (Calzetti, Kinney & Storchi-Bergmann 1994). For continuous star formation, it is thus expected that hot massive stars (which have been recently formed) are the more attenuated, while stars of lower luminosity (whose ages can span the full starburst period) can have

any attenuation. Thus age-dependent attenuation provides at once the dispersion and the trend with luminosity that are at the basis of the observed spread and tilt of the main sequence.

The observed BHeBS is also fairly well reproduced by the simulation. However, we notice that significant discrepancies remain in the colour distribution. In the three most populated bins, at magnitudes fainter than F555W $\sim$ 21.5, the model distribution is clearly bimodal. All the simulated diagrams show a gap between the main sequence and the BHeBS, which instead is much less evident (if present) in the observed CMD. This gap cannot be filled by invoking errors or by varying the attenuation. The presence of the gap is an indication the models are not able to produce extended loops during the helium-burning phase.

The sequence of red stars is also fairly well reproduced because the trend is that the attenuation is larger at larger luminosities, i.e. its slope is partially due to varying reddening across the sample.

For the number distribution between red and blue stars (R/B ratio), we notice significant discrepancies between the simulated and the observed ratios. Apart from the highest bin where no red stars are observed, the R/B ratio is underestimated by the model below F555W $= 22$, while it is largely overestimated at fainter magnitudes.

In summary, while the morphology of the simulated CMD is very similar to that of the observed one, inspection of the colour distribution shows that there are some important discrepancies, mainly concerning the evolution during the central helium-burning phase.

5.2 WLM

The CMD of WLM, depicted in the upper panel of Fig. 9, shows a broad main sequence with a quite sharp blue edge and a smoother decline in the red edge. The red sequence of WLM is poorly defined.

For WLM, we adopt a distance modulus $(m - M)_0 = 24.95$ (Gieren et al. 2008). The best simulation obtained with canonical *PARSEC* V1.1 models is shown in the middle panel of the figure. In this panel we use different colours for different ages and this helps us to interpret the main features of the CMD. The main sequence of WLM appears to span more than five magnitudes in F439W but actually, at F439W $\lesssim$ 21, it is mainly composed of blue helium-burning stars. This is very clear by looking at stars in different age ranges. In the age interval between 50 and 100 Myr (red dots), the main sequence ends at F439W $\sim$ 22.5 and the blue loop sequence is at least one magnitude brighter. At ages between 10 and 50 Myr (dark green) the main sequence ends at F439W $\sim$ 21 mag in the simulations. Brighter stars near the main sequence in this age interval are also burning central helium in the blue loop. The brightest star in the simulation is an evolved star of initial mass $M = 40$ M$_\odot$, age 5.3 Myr, luminosity $\log(L/L_\odot) = 5.77$ and effective temperature $\log(T_{\rm eff}) = 4.24$. This luminous supergiant star is not in the blue side of the loop as its fainter counterparts because, at such initial masses, helium ignition occurs just after the main sequence. Afterwards the star slowly moves towards the red supergiant phase while burning central helium (see Fig. 1). Notice that this star is brighter than the brightest star in the observed CMD but this is due to the stochastic nature of the stellar birth-rate process at these large masses. Indeed this is not the most massive star in the simulation, which is instead a main sequence star with initial mass $M = 108$ M$_\odot$ and age 1.77 Myr, about 1.3 mag fainter. In any case, it appears clearly from the simulation that the right side of the main sequence is actually blue helium-burning stars.

Also for WLM, the global luminosity function of this principal sequence is well reproduced with a SFR that increases towards

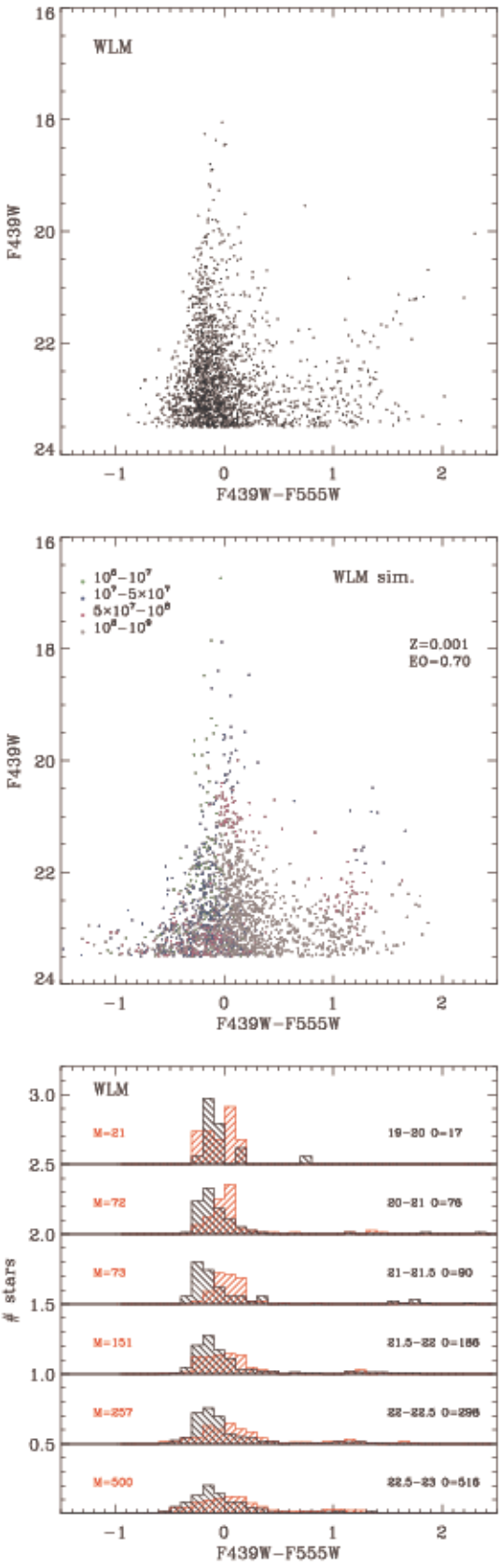

Figure 9. Upper panel: Observed CMD for WLM. Middle panel: The best model obtained with *PARSEC* V1.1. Model stars are colour-coded by age as indicated in the legend. Lower panel: Comparison of the observed and modelled colour distributions.

Table 2. Parameters of the CMD simulations of WLM.

EO	T_i [yr]	T_f [yr]	τ [yr]	X_{IMF}	$\langle SFR \rangle$ [$M_\odot$ yr^{-1}]
0.7	1×10^6	1×10^9	-5×10^8	2.65	3.7×10^{-3}
2	1×10^6	1×10^9	-5×10^8	2.35	2.7×10^{-3}
4	1×10^6	1×10^9	-2×10^8	2.35	2.9×10^{-3}

recent times (see Table 2). The average SFR in the last 100 Myr is $\langle SFR \rangle = 3.7 \times 10^{-3}$ $M_\odot$ yr^{-1}.

While the global luminosity function of the observed CMD of WLM is quite well reproduced by the simulation, inspection of the colour histograms drawn in the lower panel of Fig. 9 shows that the simulated colour distribution across the main sequence does not match the observed one. There is a clear excess of stars along the red side of the main sequence and a lack of very blue stars, which makes the simulated main sequence too broad, especially in the magnitude interval $20 \leq$ F439W ≤ 22. Note that the models adopted for WLM have the same metallicity ($Z = 0.001$) as those used for the simulation of Sextans A. In the CMD of Sextans A, the main sequence and the blue loop sequence were clearly separated, while for WLM, this separation is not so evident because of the larger errors associated with the observations. The apparent excess of red stars is due to the BHeBS, therefore we conclude that also for WLM there is a discrepancy concerning these stars.

5.3 NGC 6822

The observed CMD of NGC 6822 is shown in the upper panel of Fig. 10. With a distance modulus $(m - M)_0 = 23.31$ (Gieren et al. 2006), NGC 6822 is the nearest of the three galaxies analysed here and its observed blue sequence spans more than seven magnitudes. In the CMD, we recognize also a yellow sequence, around F439W-F555W $\sim 0.8/0.9$, and another redder sequence. It is important to clarify the origin of the yellow sequence, because the metallicity of NGC 6822, $Z \sim 0.004$, is definitely higher than that of the other two galaxies, and this sequence could trace the position of the *blue* loops of relatively metal-rich galaxies. However, our TRILEGAL simulations, and comparison of the CMD among different galaxies, indicate a large contribution from MW foreground stars near the position of the middle sequence. Actually there is some mismatch between the predicted position of the MW stars and the observed CMD. The predicted MW foreground stars not only populate the region of the observed yellow sequence (mainly thin disc stars) but also a region a few tenths of magnitude bluer. Furthermore, there is significant contamination by thin disc stars brighter than the observed F439W = 18 mag, where only a few stars are seen in the CMD. Thus, due to the significant contamination by MW stars, we exclude the yellow sequence from our analysis. Taking into account that many predicted foreground stars are slightly bluer than the observed yellow sequence, we exclude from further analysis all stars with observed colour redder than F439W − F555W = 0.6. Below this threshold the contamination becomes negligible and we may safely use the well-populated blue sequence of NGC 6822 to check the models.

The best simulation obtained with canonical *PARSEC* V1.1 models is shown in the middle panel of Fig. 10. The parameters of the stellar birth rate for this simulation are shown in Table 3. The SFR increases towards more recent times with an average value in the last 100 Myr of $\langle SFR \rangle = 3.5 \times 10^{-3}$ $M_\odot$ yr^{-1}. Note that the observed CMD includes seven *HST* fields, which cover a fraction of the galaxy (~0.73 kpc^2, see Bianchi et al. 2012b, table 1 and fig. 1).

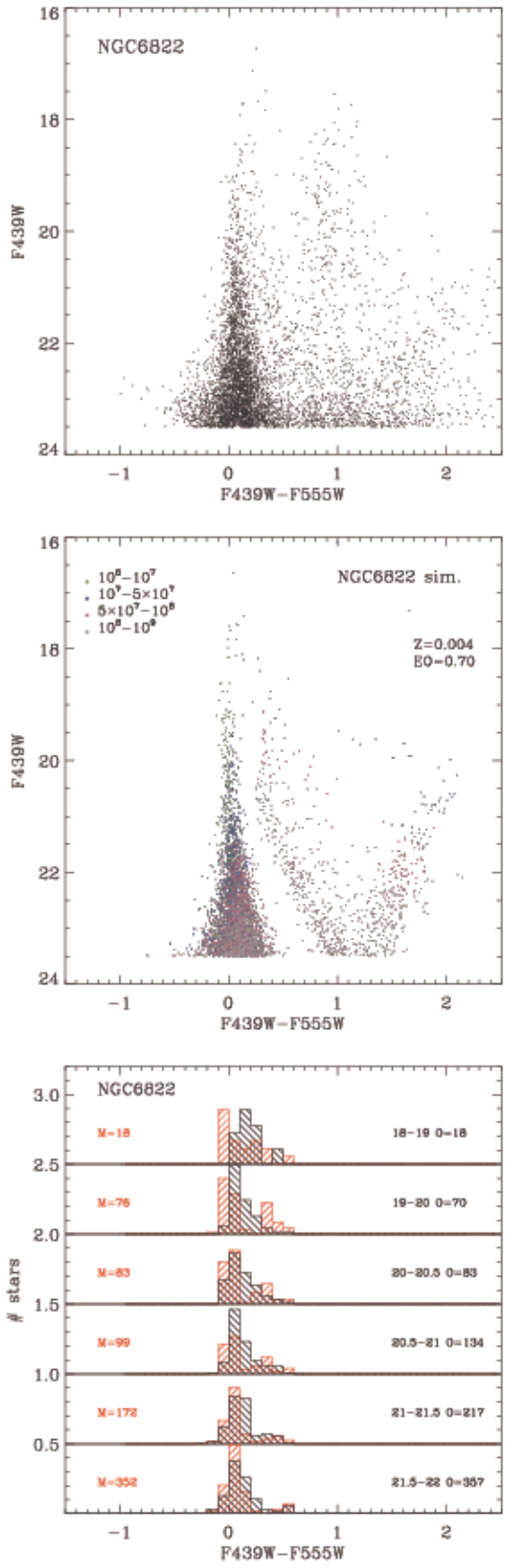

Figure 10. Upper panel: Observed CMD for NGC 6822. Middle panel: The best model obtained with *PARSEC* V1.1. Lower panel: Comparison of the observed and modelled colour distributions.

Table 3. Parameters of the CMD simulations of NGC 6822.

EO	T_i [yr]	T_f [yr]	τ [yr]	X_{IMF}	⟨SFR⟩ [$M_\odot$ yr^{-1}]
0.7	1×10^6	1×10^9	-2×10^8	2.35	3.5×10^{-3}
2	1×10^6	1×10^9	-2×10^8	2.35	3.7×10^{-3}
4	1×10^6	1×10^9	-2×10^8	2.55	4.3×10^{-3}

Because star formation is very patchy in NGC 6822, and on the other hand the *HST* pointings used here targeted star-forming sites, this SFR cannot be simply scaled to the whole galaxy (the two most conspicuous star-forming regions, including Hubble V and Hubble X, and an outer older region, were observed by Bianchi et al. 2001 and Bianchi & Efremova 2006).

We first notice that, from the *PARSEC* simulation, very few stars are expected to lie in the region occupied by the yellow sequence, corroborating the idea that this sequence is due to strong contamination by MW foreground stars. The maximum mass in the simulation is $M = 75\,M_\odot$ at an age of 2.1 Myr, while the brightest star has an initial mass $M = 72\,M_\odot$ and an age of 3.6 Myr. The simulation suggests the presence of a sequence of blue helium-burning stars running parallel to the main sequence. However, in the simulated diagram this sequence appears clearly detached from the main sequence while in the observed CMD it appears a continuation of the main sequence. This appears more clearly in the comparison of the colour distributions in the lower panel of Fig. 10. Unlike the observed distributions, the predicted ones in the range of magnitudes between $19 \leq \mathrm{F439W} \leq 21.5$ are bimodal.

6 RESULTS WITH ENHANCED ENVELOPE OVERSHOOTING MODELS

The above comparisons indicate that the adopted stellar evolutionary models cannot reproduce well the observed CMD: even accounting for errors and reddening, which tend to smear out the colour distribution, there remains a visible gap between the main sequence and the blue loop helium-burning sequence. This gap is not observed or much less evident in the data and, at the same time, the colour distribution of the models is wider than that observed. It is worth noticing that by adopting a lower metal content we

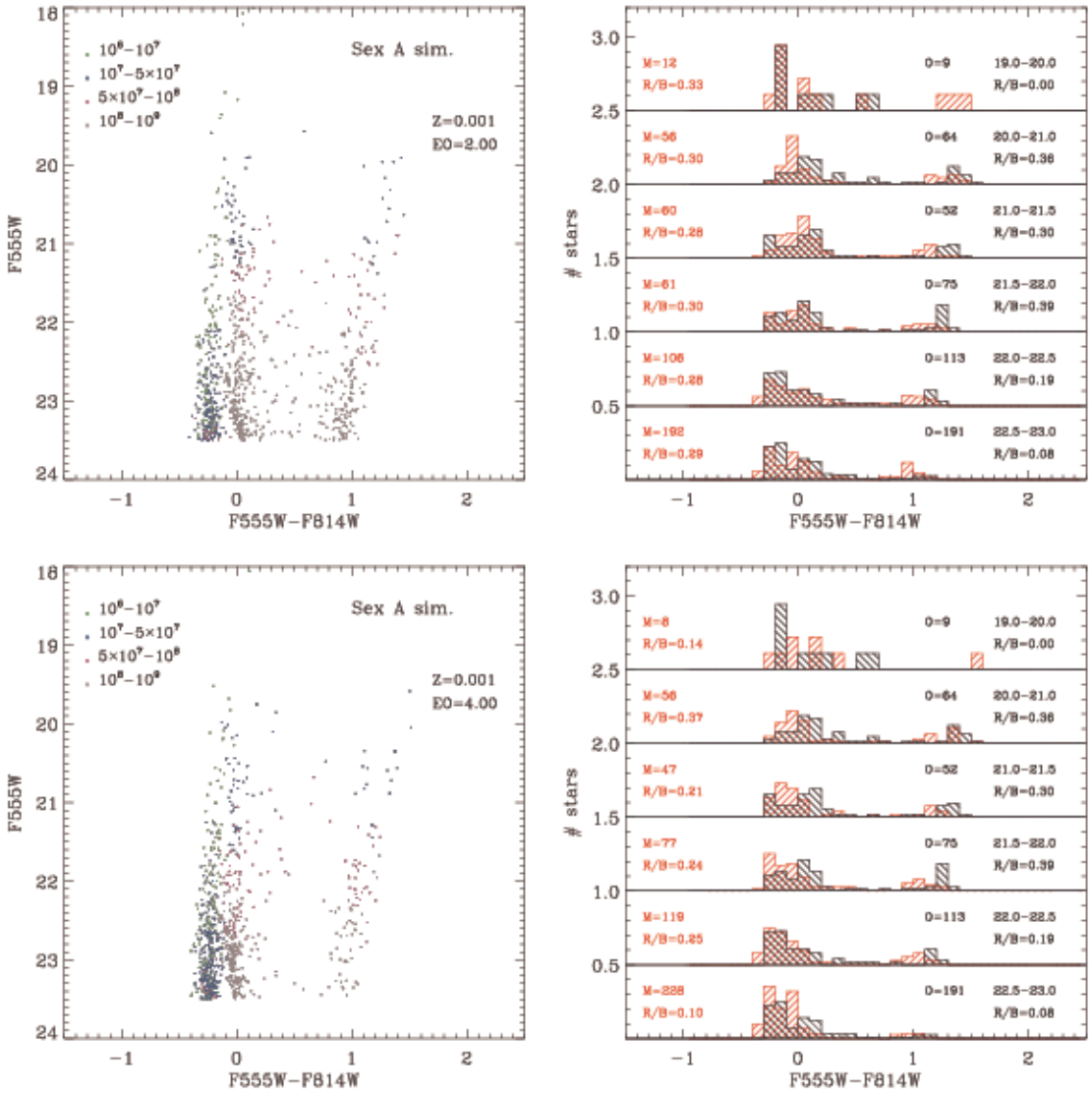

Figure 11. Upper panels: The best simulated CMD of Sextans A (left) and the corresponding star colour distribution (right), obtained with *PARSEC* after increasing the envelope overshooting to EO = $2H_P$. Lower panels: The same as in the upper panels but for a larger envelope overshooting, EO = $4H_P$.

could remove the discrepancy between the modelled and observed CMDs, but this would require a metallicity value quite discrepant from the one determined from spectroscopic observations. Moreover, the value adopted in the simulations of WLM and Sextans A, $Z = 0.001$, lies between the ones derived observationally for the two galaxies, indicating that the origin of the discrepancy is not due to the adoption of a too high metallicity. Given the inability of reproducing the observed blue loops using models with canonical envelope overshooting, we repeated the simulations adopting models with enhanced envelope overshooting.

The best simulations of Sextans A obtained with models with enhanced envelope overshooting are shown in the upper and lower panels of Fig. 11 for EO $= 2H_P$ and EO $= 4H_P$, respectively. As already discussed in Section 2.5, models with enhanced envelope overshooting produce more extended blue loops and this is visible in the corresponding simulations. Adopting EO $= 2H_P$ produces a reasonably good fit to the observed CMD of Sextans A. The bimodal behaviour noticed in Fig. 8 at fainter magnitudes disappears and the excess of stars in the red side of the main sequence becomes significantly less pronounced. With EO $= 4H_P$, the loops are even more extended and the predicted main sequence becomes even narrower than the observed one. The SFR is not significantly different from the one derived with the standard *PARSEC* V1.1 models. It increases by about 16 per cent using the models with EO $= 2H_P$ and by another 10 per cent if one consider the models with EO $= 4H_P$. The latter increase is in part due to the decrease of the star formation timescale adopted for the best fit (Table 1).

The observed CMD of Sextans A is so well populated along the different sequences that we may gain some insight into the properties of the different mixing models by analysing the number ratios between red [F555W − F814W > 0.6 and F555W − F814W < (31.2 − F555W)/7] and blue stars (F555W − F814W ≤ 0.6). The observed number ratios are plotted against the apparent magnitude in Fig. 12 with large filled dots. The number ratios predicted by adopting the different values of the overshooting scale are plotted with different symbols and colours and are labelled with the adopted overshooting scale. The size of the envelope overshooting affects not only the extension of the loop but also the relative lifetimes in the blue and red sides. In the models with larger envelope overshooting, the loops begin at earlier times during central helium burning (Fig. 3), and the relative number of red to blue stars decreases. The observed number ratios of stars in the red and blue sides of the loops have been already used to check the performance of stellar evolution models, because they concern post main-sequence phases, hence they depend almost exclusively on the lifetime ratios of the stars in the corresponding phases (e.g. Dohm-Palmer & Skillman 2002). We cannot perform the same comparison here because we cannot disentangle the blue side of the loop and the main sequence. Indeed, in Fig. 12 we plot the ratios between the number of red stars and blue stars including also the main sequence stars. Thus, these ratios are not strictly related to the above lifetime ratios not only because they include the main sequence phase but also because, by selecting them in bins of constant magnitude, we are including stars with different masses. Nevertheless, the exercise is meaningful because we are simulating the real evolution of these stars in the CMD. Indeed the figure shows that, for higher envelope overshooting, the R/B ratio decreases significantly, because the red side of the loops becomes less and less populated.

The best simulation of WLM obtained with these new models is shown in Fig. 13 for EO $= 2H_P$ and EO $= 4H_P$. Again for WLM, the simulations performed with enhanced envelope overshooting models better agree with the observations. The relative excess of

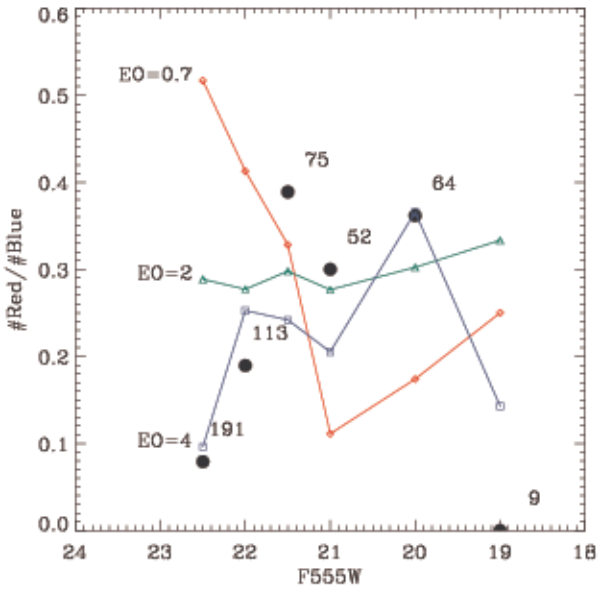

Figure 12. Observed (large filled dots) and predicted (coloured lines with symbols) ratios between the number of stars redder and bluer than F555W − F814W = 0.6 as a function of the apparent magnitude, in the CMDs of Sextans A. The numbers indicate the total number of stars observed in each magnitude bin. The predicted ratios are labelled with the envelope overshooting values.

stars in the red side of the main sequence decreases significantly with EO $= 2H_P$ and almost disappears with EO $= 4H_P$. Compared with the standard case of EO $= 0.7H_P$, the average SFR in the new best-match models is about 30 per cent lower. This is due to the different IMF slope adopted in the first case, $x = 2.65$, with respect to the one adopted in the latter cases $x = 2.35$.

For NGC 6822, the best simulations obtained with models with enhanced envelope overshooting are shown in the upper and lower panels of Fig. 14, for EO $= 2H_P$ and EO $= 4H_P$, respectively. Even in this case, the morphology of the blue sequence is better reproduced.

7 CONCLUSIONS

With the aim of extending the new library of stellar evolutionary tracks and isochrones computed with *PARSEC*, we begin the calculation of new evolutionary tracks of massive stars. We adopt the same input physics used in the *PARSEC* V1.1 published version of low and intermediate mass stars, the only difference being that for masses $M \geq 14$ M$_\odot$ we include mass loss. The new calculations supersede the old stellar evolution tracks of massive stars (Bertelli et al. 1994), so that we now provide updated and homogeneous sets of evolutionary tracks from very low ($M = 0.1$ M$_\odot$) to very massive ($M = 350$ M$_\odot$) stars, from the pre-main sequence to the beginning of central carbon burning.

In this paper, we presented new evolutionary tracks of low metallicity, $Z = 0.001$ and $Z = 0.004$. We also compared the new tracks with observed CMDs of star-forming regions in three selected nearby metal-poor dwarf irregular galaxies, Sextans A, WLM and NGC 6822. These galaxies are dominated by the last ongoing starburst and the existing *HST* CMDs are a useful workbench for testing the overall performance of stellar evolution tracks in the domain of intermediate and massive stars. The contamination by MW dwarf stars, estimated with TRILEGAL simulations, is negligible in Sextans A and WLM, while for NGC 6822 it is significant at colours

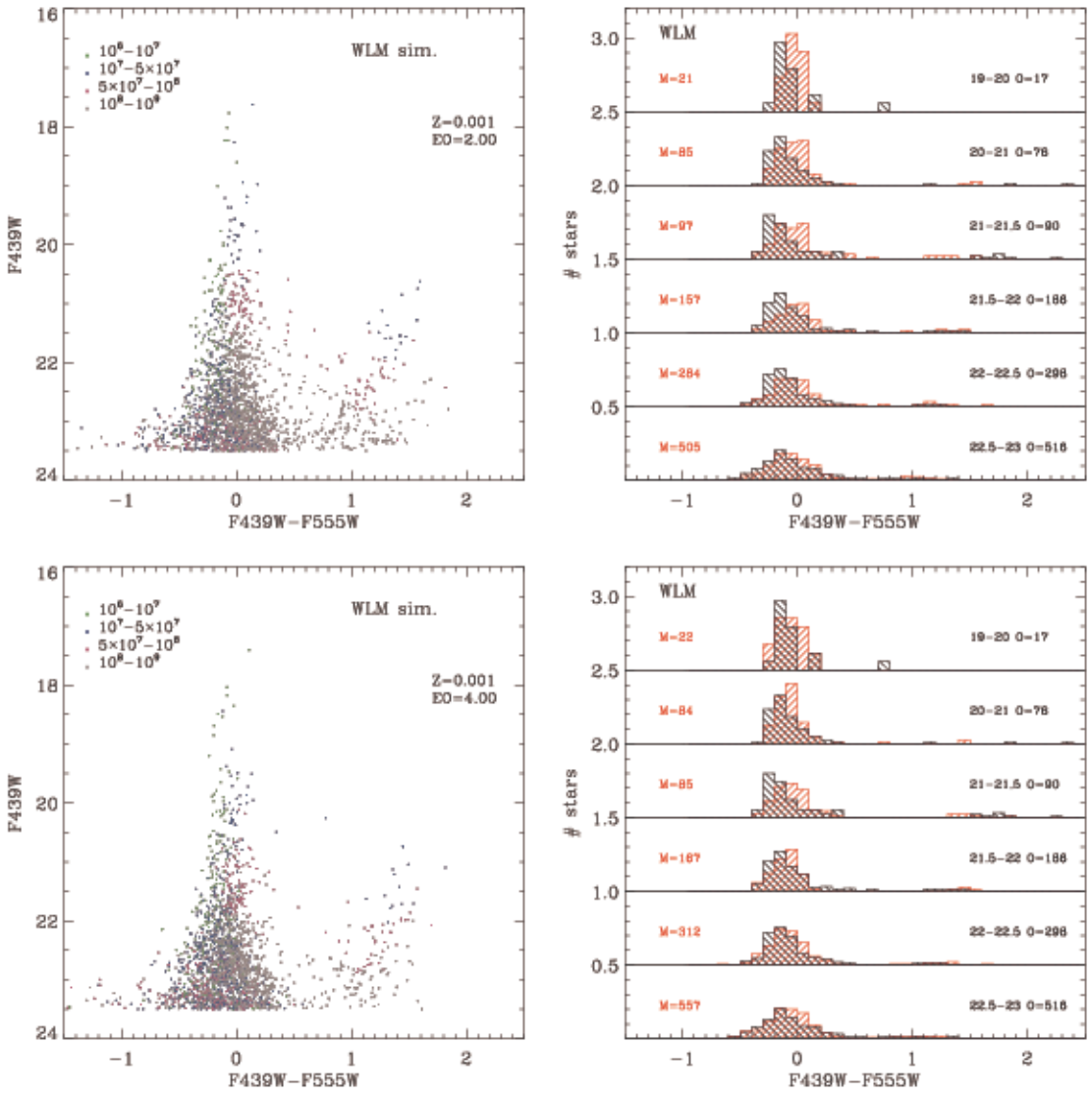

Figure 13. Upper panels: The best simulated CMD of WLM (left) and the corresponding star colour distribution (right), obtained with *PARSEC* after increasing the envelope overshooting to EO = $2H_P$. Lower panels: The same as in the upper panels but for a larger envelope overshooting, EO = $4H_P$.

F439W − F555W ≥ 0.6: for this galaxy we used only bluer stars, which include the main sequence and the BHeBS.

Since the new massive star tracks have not yet been implemented in the popular CMD simulators (e.g. TRILEGAL) we built our own CMD simulator, where we specify the IMF and SFR laws, the metallicity, the photometric errors, attenuation and binary effects. In the simulations, we fix the metallicity to the value that is the nearest to that found in literature for the youngest populations of the galaxy, either stars or gas. This is important because our aim is to check the model results using the morphology of the CMD, in particular of the BHeBS, which is known to depend significantly on the metallicity. The photometric errors are taken from the published photometry catalogues and are reproduced statistically as a function of the apparent magnitude. As for the attenuation by interstellar dust, we exploit the advantage that it has been individually derived for a large sub-sample of stars, using a star-by-star multi-band spectro-photometric analysis (Bianchi et al. 2012b). In all three galaxies, the attenuation is characterized by an average value that rises with the intrinsic luminosity for the hot stars and by a significant dispersion, which is consistent with an age-selective extinction together with local variations of the dust content. Only by including such a dispersion and trend with luminosity, could we reproduce the morphology of the different sequences seen in the CMD, without a real need to use any dispersion of the metallicity. This is especially true for Sextans A, where the photometric errors are very small, while for NGC 6822, there is still room for dispersion of the metallicity, which indeed has been observed in this galaxy, and is not surprising given its patchy star-formation episodes. We check also the effects of non-physical binaries and find that they are not very significant so that we do not discuss them in the paper.

For Sextans A and WLM, we adopted a metallicity $Z = 0.001$, which is an upper limit for the former and a lower limit for the latter. In both galaxies the location of the main sequence is well reproduced by the new tracks. Sextans A shows a well-populated red sequence, which is also fairly well reproduced by the new models. For Sextans A, the main sequence and BHeBS form two parallel vertical sequences while in WLM they form a broad blue sequence. All models generally reproduce these sequences but a quantitative comparison of the colour distribution in different magnitude bins shows that, for models with canonical overshooting, the

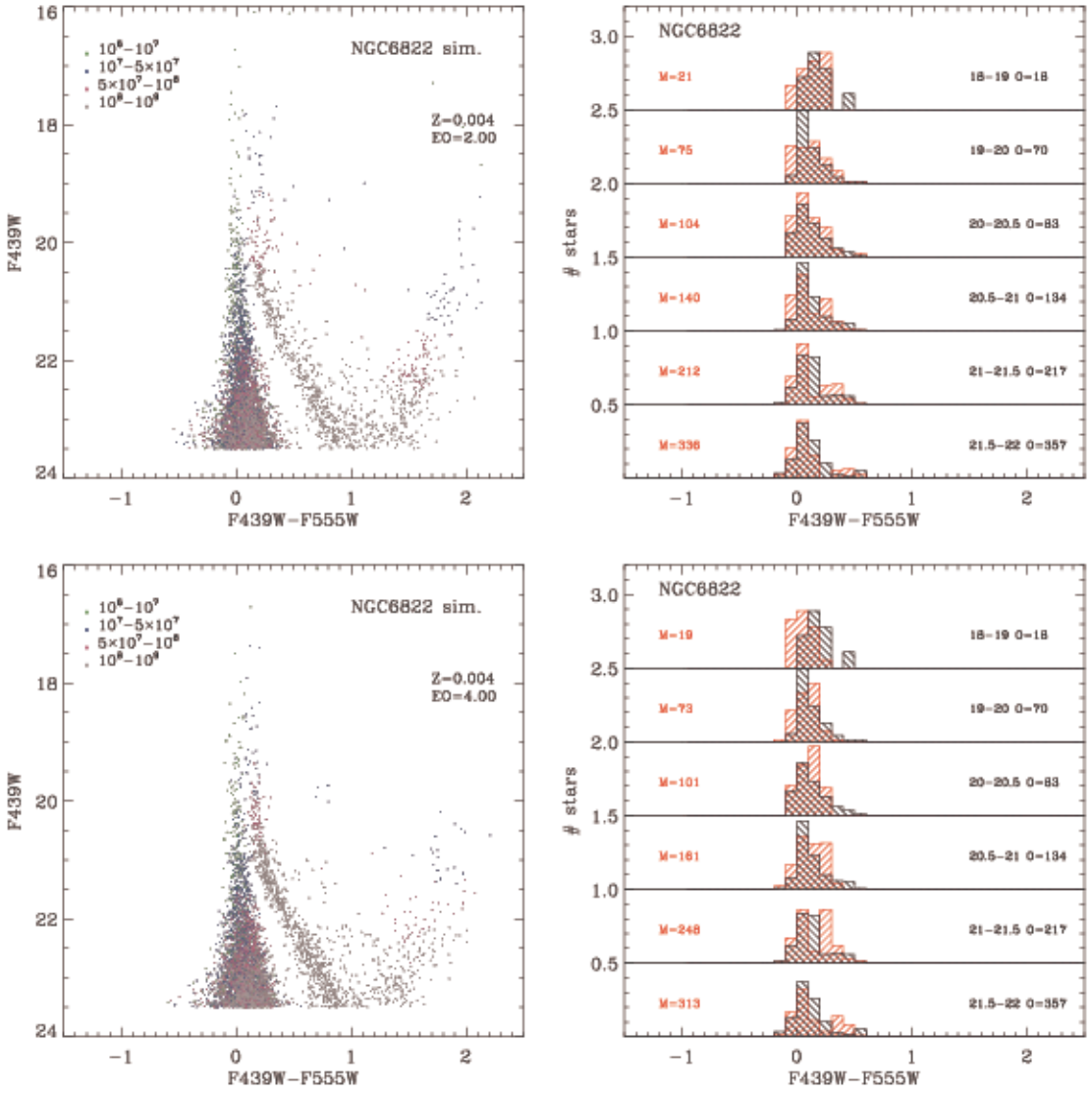

Figure 14. Upper panels: The best simulated CMD of NGC 6822 (left) and the corresponding star colour distribution (right), obtained with *PARSEC* after increasing the envelope overshooting to EO = $2H_P$. Lower panels: The same as in the upper panels but for a larger envelope overshooting, EO = $4H_P$.

simulated distributions are broader than the observed ones and generally skewed towards redder colours, in both galaxies. A lower metallicity, which would render the blue loops more extended, would be discrepant with measured values, therefore we interpret this mismatch as evidence that the BHeBSs predicted by the models are not hot enough.

For NGC 6822, we adopt a metallicity of $Z = 0.004$. As for the previous galaxies, the fit of the main sequence is fairly good, but at this metallicity the problem of the blue loops is even more exacerbated. The models computed with *PARSEC* V1.1 (canonical overshooting) show a shortening of the loops above $\log(L/L_\odot) \sim 3.5$ (Fig. 2) and the corresponding simulation shows a blue sequence with bimodal colour distribution, which is not evident in the observed CMD. This corroborates the notion that even at $Z = 0.004$ the BHeBSs predicted by the models are not hot enough and that, to reproduce the observed morphology of the CMD with the *PARSEC* V1.1 prescriptions, a metallicity much lower than the measured values would be required.

We show that this discrepancy is overcome by extending the overshooting at the base of the convective envelope. The simulations made with the enhanced EO models better reproduce the observed CMDs for all three galaxies. For Sextans A, the comparison can be extended to the number ratios between stars in the red side of the loop and blue stars (including also main sequence stars). The comparison with the observed ratios strongly support the largest value, EO = $4H_P$. Thus there is evidence that an EO larger than that adopted in *PARSEC* V1.1 should be preferred. Apart from the morphology (and corresponding luminosity function) of the loops, there are no other significant differences between models computed with different EO scales. The SFR, estimated from the best-match model in each case, increases by less than ∼15 per cent at increasing EO mixing, and so it is not significantly affected by the choice of this parameter. We also find that a Salpeter slope for intermediate and massive stars is, in general, the preferred choice to reproduce the observed luminosity function.

Notice that the mixing scales required to reproduce the observed loops, EO = $2H_P$ or EO = $4H_P$, are definitely larger than the maximum values compatible with, e.g. the location of the RGB bump in evolved low mass stars, which can be well reproduced by an envelope overshooting not exceeding EO = $0.7H_P$, the value adopted

in *PARSEC* V1.1 for intermediate mass stars. Thus the results suggest a strong dependence of the mixing scale below the formal Schwarzschild border of the outer envelope on the mass or luminosity of the star. A possible mechanism for such enhanced mixing could be the large discontinuity in angular momentum that develops between the outer envelope and the inner core during the first dredge-up, when stellar rotation is included. The shear generated by this discontinuity could give rise to the required enhancement. However, it is interesting to note that current models that consistently include rotational mixing in the whole star interiors, do not show larger loops (Heger & Langer 2000; Georgy et al. 2013), and thus would face the same difficulty. More extended loops could be possibly obtained by adopting the Ledoux criterion instead of the Schwarzschild one, because the former is known to favour the development of loops, at least in the domain of massive stars (Chiosi & Summa 1970). Though disfavoured by the analysis of Kato (1966), the Ledoux criterion has recently received some observational support (Georgy, Saio & Meynet 2014), and its consequences are worth exploring systematically. All this renders the problem of the blue loops and the origin of such enhanced mixing quite challenging. Our simulations support the possibility that, with a mild efficiency of convective core overshooting, the mixing by the first dredge-up becomes more efficient at increasing luminosity, and could reach a few pressure scale heights below the formal Schwarzschild border, in the domain of intermediate and massive stars. In the future we will perform the same comparison with galaxies of different metallicity, a work that is already in progress. Furthermore, it is worth testing models that use different schemes, such as rotational mixing and/or a diffusive approach to overshooting, to see if other mixing schemes are able to produce internal chemical H profiles that allow the development of more extended loops.

ACKNOWLEDGEMENTS

This work was based on observations made with the *HST*, programmes HST-GO 11079 and 10915. We thank M Barbieri, ZY Cai, S Charlot, Y Chen, A Grotsch-Noels, M Mapelli, M Spera and S Zaggia for helpful discussions. We thank the anonymous referee for useful suggestions. PM acknowledges support from *Progetto di Ateneo 2012*, University of Padova, ID: CPDA125588/12.

REFERENCES

Alongi M., Bertelli G., Bressan A., Chiosi C., 1991, A&A, 244, 95
Asplund M., Grevesse N., Sauval A. J., Allende Prieto C., Kiselman D., 2004, A&A, 417, 751
Asplund M., Grevesse N., Sauval A. J., Scott P., 2009, ARA&A, 47, 481
Bertelli G., Bressan A. G., Chiosi C., 1985, A&A, 150, 33
Bertelli G., Bressan A., Chiosi C., Fagotto F., Nasi E., 1994, A&AS, 106, 275
Bertelli G., Nasi E., Girardi L., Marigo P., 2009, A&A, 508, 355
Bianchi L., Efremova B. V., 2006, AJ, 132, 378
Bianchi L., Scuderi S., Massey P., Romaniello M., 2001, AJ, 121, 2020
Bianchi L., Efremova B., Hodge P., Kang Y., 2012a, AJ, 144, 142
Bianchi L., Efremova B., Hodge P., Massey P., Olsen K. A. G., 2012b, AJ, 143, 74
Böhm-Vitense E., 1958, Zeitschrift fur Astrophysik, 46, 108
Bouret J.-C., Lanz T., Martins F., Marcolino W. L. F., Hillier D. J., Depagne E., Hubeny I., 2013, A&A, 555, A1
Bresolin F., Pietrzyński G., Urbaneja M. A., Gieren W., Kudritzki R.-P., Venn K. A., 2006, ApJ, 648, 1007
Bressan A. G., Chiosi C., Bertelli G., 1981, A&A, 102, 25
Bressan A., Fagotto F., Bertelli G., Chiosi C., 1993, A&AS, 100, 647
Bressan A., Marigo P., Girardi L., Salasnich B., Dal Cero C., Rubele S., Nanni A., 2012, MNRAS, 427, 127
Bressan A., Marigo P., Girardi L., Nanni A., Rubele S., 2013, European Phys. J. Web Conf., 43, 3001
Brunish W. M., Becker S. A., 1990, ApJ, 351, 258
Caffau E., Ludwig H.-G., Steffen M., Freytag B., Bonifacio P., 2011, Sol. Phys., 268, 255
Calzetti D., Kinney A. L., Storchi-Bergmann T., 1994, ApJ, 429, 582
Cardelli J. A., Clayton G. C., Mathis J. S., 1989, ApJ, 345, 245
Castelli F., Kurucz R. L., 2003, in Piskunov N., Weiss W. W., Gray D. F., eds, IAU Symp. Vol. 210, Modelling of Stellar Atmospheres, p. 20P
Chabrier G., 2001, ApJ, 554, 1274
Chen Y., Girardi L., Bressan A., Marigo P., Barbieri M., Kong X., 2014a, MNRAS, 444, 2525
Chiosi C., Summa C., 1970, Ap&SS, 8, 478
Christensen-Dalsgaard J., Monteiro M. J. P. F. G., Rempel M., Thompson M. J., 2011, MNRAS, 414, 1158
Cioni M.-R. L., Habing H. J., 2005, A&A, 429, 837
Cyburt R. H. et al., 2010, ApJS, 189, 240
Dalcanton J. J. et al., 2009, ApJS, 183, 67
Davidge T. J., 2003, PASP, 115, 635
de Jager C., Nieuwenhuijzen H., van der Hucht K. A., 1988, A&AS, 72, 259
Deheuvels S. et al., 2010, A&A, 514, A31
Dewitt H. E., Graboske H. C., Cooper M. S., 1973, ApJ, 181, 439
Dohm-Palmer R. C., Skillman E. D., 2002, AJ, 123, 1433
Dolphin A. E. et al., 2003a, AJ, 125, 1261
Dolphin A. E. et al., 2003b, AJ, 126, 187
Fagotto F., Bressan A., Bertelli G., Chiosi C., 1994a, A&AS, 104, 365
Fagotto F., Bressan A., Bertelli G., Chiosi C., 1994b, A&AS, 105, 29
Fagotto F., Bressan A., Bertelli G., Chiosi C., 1994c, A&AS, 105, 39
Georgy C. et al., 2013, A&A, 558, A103
Georgy C., Saio H., Meynet G., 2014, MNRAS, 439, L6
Gieren W., Pietrzyński G., Nalewajko K., Soszyński I., Bresolin F., Kudritzki R.-P., Minniti D., Romanowsky A., 2006, ApJ, 647, 1056
Gieren W. et al., 2008, ApJ, 683, 611
Girardi L., Bressan A., Bertelli G., Chiosi C., 2000, A&AS, 141, 371
Girardi L., Bertelli G., Bressan A., Chiosi C., Groenewegen M. A. T., Marigo P., Salasnich B., Weiss A., 2002, A&A, 391, 195
Girardi L., Groenewegen M. A. T., Hatziminaoglou E., da Costa L., 2005, A&A, 436, 895
Girardi L., Rubele S., Kerber L., 2009, MNRAS, 394, L74
Godart M., Noels A., Scuflaire R., 2013, European Phys. J. Web Conf., 43, 1008
Gordon K. D., Clayton G. C., 1998, ApJ, 500, 816
Graboske H. C., Dewitt H. E., Grossman A. S., Cooper M. S., 1973, ApJ, 181, 457
Gräfener G., Hamann W.-R., 2008, A&A, 482, 945
Grevesse N., Sauval A. J., 1998, Space Sci. Rev., 85, 161
Groh J. H., Meynet G., Ekström S., Eggenberger P., Georgy C., Granada A., Heap S., 2013, EAS Publ. Series, 60, 51
Haft M., Raffelt G., Weiss A., 1994, ApJ, 425, 222
Halabi G. M., El Eid M. F., Champagne A., 2012, ApJ, 761, 10
Heger A., Langer N., 2000, ApJ, 544, 1016
Hodge P., Miller B. W., 1995, ApJ, 451, 176
Humphreys R. M., Davidson K., 1979, ApJ, 232, 409
Iben I., Jr, 1966, ApJ, 143, 483
Iglesias C. A., Rogers F. J., 1996, ApJ, 464, 943
Itoh N., Kohyama Y., 1983, ApJ, 275, 858
Itoh N., Uchida S., Sakamoto Y., Kohyama Y., Nozawa S., 2008, ApJ, 677, 495
Kamath D., Wood P. R., Soszyński I., Lebzelter T., 2010, MNRAS, 408, 522
Kamath D., Karakas A. I., Wood P. R., 2012, ApJ, 746, 20
Kang A. et al., 2006, A&A, 454, 717
Kato S., 1966, PASJ, 18, 374
Kaufer A., Venn K. A., Tolstoy E., Pinte C., Kudritzki R.-P., 2004, AJ, 127, 2723

Kennicutt R. C., Jr 1998, in Gilmore G., Howell D., eds, ASP Conf. Ser. Vol. 142, The Stellar Initial Mass Function (38th Herstmonceux Conference). Astron. Soc. Pac., San Francisco, p. 1
Kniazev A. Y., Grebel E. K., Pustilnik S. A., Pramskij A. G., Zucker D. B., 2005, AJ, 130, 1558
Lauterborn D., Refsdal S., Weigert A., 1971, A&A, 10, 97
Lee H., Skillman E. D., Venn K. A., 2005, ApJ, 620, 223
Lodders K., Palme H., Gail H.-P., 2009, in Trümper J.E., ed., Landolt-Börnstein-Group VI Astronomy and Astrophysics Numerical Data and Functional Relationships in Science and Technology Vol. 4B: Solar system, p. 44
Maeder A., Przybilla N., Nieva M.-F., Georgy C., Meynet G., Ekström S., Eggenberger P., 2014, A&A, 565, A39
Marigo P., Aringer B., 2009, A&A, 508, 1539
Marigo P., Girardi L., Bressan A., Groenewegen M. A. T., Silva L., Granato G. L., 2008, A&A, 482, 883
Martins F., Palacios A., 2013, A&A, 560, A16
Misselt K. A., Clayton G. C., Gordon K. D., 1999, ApJ, 515, 128
Muijres L., Vink J. S., de Koter A., Hirschi R., Langer N., Yoon S.-C., 2012, A&A, 546, A42
Munakata H., Kohyama Y., Itoh N., 1985, ApJ, 296, 197
Nugis T., Lamers H. J. G. L. M., 2000, A&A, 360, 227
Pagel B. E. J., Edmunds M. G., Smith G., 1980, MNRAS, 193, 219
Richer M. G., McCall M. L., 1995, ApJ, 445, 642
Sibbons L. F., Ryan S. G., Cioni M.-R. L., Irwin M., Napiwotzki R., 2012, A&A, 540, A135
Silva L., Granato G. L., Bressan A., Danese L., 1998, ApJ, 509, 103
Skillman E. D., Kennicutt R. C., Hodge P. W., 1989, ApJ, 347, 875
Skillman E. D., Terlevich R., Melnick J., 1989, MNRAS, 240, 563
Tolstoy E., Irwin M. J., Cole A. A., Pasquini L., Gilmozzi R., Gallagher J. S., 2001, MNRAS, 327, 918
Torres G., Vaz L. P. R., Sandberg Lacy C. H., Claret A., 2014, AJ, 147, 36
Urbaneja M. A., Kudritzki R.-P., Bresolin F., Przybilla N., Gieren W., Pietrzyński G., 2008, ApJ, 684, 118
Venn K. A. et al., 2001, ApJ, 547, 765
Venn K. A., Tolstoy E., Kaufer A., Skillman E. D., Clarkson S. M., Smartt S. J., Lennon D. J., Kudritzki R. P., 2003, AJ, 126, 1326
Vink J. S., de Koter A., Lamers H. J. G. L. M., 2000, A&A, 362, 295
Vink J. S., de Koter A., Lamers H. J. G. L. M., 2001, A&A, 369, 574
Vink J. S., Muijres L. E., Anthonisse B., de Koter A., Gräfener G., Langer N., 2011, A&A, 531, A132
Weiss A., Serenelli A., Kitsikis A., Schlattl H., Christensen-Dalsgaard J., 2005, A&A, 441, 1129
Woosley S. E., Heger A., 2012, ApJ, 752, 32
Xu H. Y., Li Y., 2004, A&A, 418, 225

This paper has been typeset from a TEX/LATEX file prepared by the author.